

Evaluation of Metal Fuel for Use in Light Water Reactors Utilizing the BISON Code Final Report

DOE Award DE-NE0009041

September 1, 2022

Author(s)

Wenfeng Liu, Joe Rashid, Michael Kennard, and Bill Lyon
Structural Integrity Associates, Inc.

Brian Wirth
University of Tennessee - Knoxville

ABSTRACT

The report summarized the research work performed using BISON fuel performance code to model the behavior of a helical four-lobe geometry metal fuel with co-extruded U-Zr alloy fuel core and Zr-Nb cladding, a fuel design from Lightbridge Corp., in Light Water Reactor environment. A few new material models for the fuel material have been adopted/developed using open literature data and implemented in BISON code. In addition, code modifications were made to improve the material models and to enhance BISON's efficiency in modeling this special fuel design using finite element methodology. Current study examines the fuel behavior in normal operation and accident scenarios with either a loss of coolant or a rapid power increase using a few idealized cases. In comparison to the dominant ceramic UO_2 fuel type in LWRs, metal fuel shows enhanced safety in accident conditions, as expected. However, the material behavior and design features of this metal fuel show challenges that differ from those for the ceramic fuel; specifically, fuel utilization could be limited by the dimensional changes from fuel swelling and its synergy with reduced cladding ductility due to corrosion and irradiation. A few notable features observed from the modeling results, attributable to the special geometry, namely, non-uniform heat flux and corrosion, are highlighted and discussed. Data from future experimental programs are expected to improve upon the present code/model validation and further ascertain this metal fuel attributes and performance limitations.

CONTENTS

| | |
|---|----|
| Abstract | i |
| Contents | ii |
| List of Figures | iv |
| List of Tables | vi |
| 1. Introduction..... | 1 |
| 2. Material Model Development | 5 |
| 2.1 U-Zr Material Models | 5 |
| 2.1.1 Thermal Conductivity..... | 5 |
| 2.1.2 Heat Capacity | 8 |
| 2.1.3 Creep..... | 9 |
| 2.1.4 Density..... | 12 |
| 2.1.5 Elastic Modulus | 12 |
| 2.1.6 Phase Transition | 13 |
| 2.1.7 Yield Strength..... | 13 |
| 2.1.8 Thermal Expansion..... | 16 |
| 2.1.9 Fuel Swelling..... | 17 |
| 2.2 Zr-Nb Cladding Alloy Models..... | 19 |
| 2.3 Coolant Channel Model | 24 |
| 3. BISON Modeling | 26 |
| 3.1 Finite Element Models..... | 26 |
| 3.2 BISON Code Modification | 28 |
| 4. Modeling Results For Normal Operation | 29 |
| 4.1 Base Case Description | 29 |
| 4.2 Results..... | 30 |
| 4.2.1 Burnup | 30 |
| 4.2.2 Fuel Temperature..... | 30 |
| 4.2.3 Cladding Corrosion | 32 |
| 4.2.4 Dimensional Changes..... | 33 |
| 4.2.5 Cladding Stresses/Strains | 35 |
| 4.3 Performance Metrics | 37 |
| 5. Modeling Results In Accident Conditions..... | 39 |
| 5.1 LOCA Modeling | 39 |
| 5.1.1 LOCA Case Description..... | 39 |
| 5.1.2 LOCA Modeling Results | 41 |
| 5.2 REA Modeling..... | 44 |
| 5.2.1 REA HFP Case | 44 |
| 5.2.2 REA HFP Results | 45 |
| 5.2.3 REA HZP Case..... | 48 |
| 5.2.4 REA HZP Results..... | 49 |
| 5.2.5 Fuel Failure Discussion | 51 |

| | |
|---|----|
| 6. Conclusions | 53 |
| 7. Acknowledgement | 55 |
| 8. References | 56 |
| Appendix A Script for Computing Geometry Parameters of Helical Four-Lobe Fuel | 60 |
| Appendix B Materials Block in BISON Input | 65 |
| Appendix C Mesh Generation Scripts | 68 |

LIST OF FIGURES

| | |
|--|----|
| Figure 1: Schematic of Lightbridge metallic fuel design [11]..... | 2 |
| Figure 2: Cross section view of Lightbridge metallic fuel design [13] | 3 |
| Figure 3: Measured thermal conductivity of U-Zr alloy [5] | 6 |
| Figure 4: Comparison between thermal conductivity models of UZr_2 | 7 |
| Figure 5: Fuel temperature prediction using UTK model in BISON..... | 7 |
| Figure 6: Comparison between different specific heat models for modeling UZr_2 alloy | 8 |
| Figure 7: Enthalpy of UZr_2 versus temperature..... | 9 |
| Figure 8: Fitting measured data of UZr_2 to a power-law creep model | 9 |
| Figure 9: Comparison between Kutty model and BISON models at 35 MPa | 10 |
| Figure 10: Fitting measured creep rate of UZr_2 alloy to a power-law creep model | 11 |
| Figure 11: Elastic modulus of UZr_2 as a function of temperature | 12 |
| Figure 12: Zirconium-uranium phase diagram [6]..... | 13 |
| Figure 13: Ultimate tensile strength and yield strength of U-Zr alloy at room temperature | 14 |
| Figure 14: Yield strength of U-Zr alloy at 370°C | 14 |
| Figure 15: Uniform elongation of U-Zr at room temperature..... | 15 |
| Figure 16: Measured hardness of UZr_2 versus temperature [5]..... | 15 |
| Figure 17: Comparison of yield strength between UZr_2 and MATPRO Zry model..... | 16 |
| Figure 18: Linear thermal expansion strain versus temperature..... | 17 |
| Figure 19: Volume change versus temperature for U-Zr alloys containing up to 22 wt% uranium [6] | 18 |
| Figure 20: Model of gaseous swelling rate versus burnup for 10 μm grain size..... | 19 |
| Figure 21: Model of gaseous swelling rate versus burnup for 130 μm grain size..... | 19 |
| Figure 22: Non-uniform oxidation predicted by BISON code using a) Zr-4 model and b) A newly implemented Zr-Nb oxidation model..... | 21 |
| Figure 23: Power law representation of oxidation kinetics. Left: Power law fit of the pre-transition regime of ZIRLO sheet alloy [47]; Right: Exponent n from pre-transition (or pre-breakaway) power law fits of the different alloys [48]. | 22 |
| Figure 24: Hydrogen content versus corrosion weight gain (proportional to oxide thickness) during autoclave testing of various alloys in pure water at 360°C [46-47]..... | 23 |
| Figure 25: Hydrogen uptake versus weight gain for Zr-1Nb (Pink lines) | 24 |
| Figure 26: Comparison of cladding heat flux from BISON and PEGASUS code | 24 |
| Figure 27: 2-D finite element grid for four-lobe metal fuel..... | 26 |
| Figure 28: 2-D multi-slice grid for helical four-lobe metal fuel | 27 |
| Figure 29: 3-D rod segment grids for helical four-lobe metal fuel..... | 27 |
| Figure 30: Temperature contour of a multi-slice geometry using modified coolant channel model.. | 28 |
| Figure 31: Rod average LHGR for the modeling case | 29 |
| Figure 32: Axial peaking factors at different times | 29 |
| Figure 33: Temperatures at centerline, cladding valley and tip at mid-height location | 31 |
| Figure 34: Axial profile of centerline temperature in comparison to UO_2 fuel at BOL | 31 |
| Figure 35: Comparison of centerline temperatures with different fuel configurations | 31 |
| Figure 36: Non-uniform cladding oxidation at mid-height location..... | 32 |
| Figure 37: Axial cladding oxidation profile in comparison to UO_2 fuel | 33 |
| Figure 38: Fuel deformation in comparison to original contour (in pink curve) | 33 |
| Figure 39: Axial strain contour in different fuel components at EOL..... | 34 |
| Figure 40: Comparison of fuel swelling with different geometries in 2-D cases | 35 |
| Figure 41: Cladding von-Mises stress contour at the EOL..... | 35 |
| Figure 42: Cladding von-Mises stress at the valley location | 36 |

| | |
|--|----|
| Figure 43: Cladding von-Mises stress at the lobe tip location..... | 36 |
| Figure 44: Cladding hoop strain at the valley and lobe tip locations..... | 37 |
| Figure 45: Cladding axial strain at the valley and lobe tip locations..... | 37 |
| Figure 46: Decay power using ANS model (LHGR = 45 kW/m) | 39 |
| Figure 47: Coolant pressure in the simulated LOCA condition | 40 |
| Figure 48: Axial power profile in the LOCA condition | 40 |
| Figure 49: Clad surface heat transfer coefficient in a simulated LOCA condition at valley location (peak power = 45 kW/m, flooding time = 5 sec) | 41 |
| Figure 50: Cladding surface temperature during LOCA (power = 30 kW/m, flooding time = 5 sec) | 41 |
| Figure 51: Cladding surface temperature during LOCA (power = 45 kW/m, flooding time = 5 sec) | 42 |
| Figure 52: Cladding surface temperature during LOCA (power = 45 kW/m, flooding time = 20 sec) | 42 |
| Figure 53: Cladding surface temperature during LOCA (power = 45 kW/m, flooding time = 60 sec) | 42 |
| Figure 54: Von-Mises stress contour at the time of PCT (power = 45 kW/m, flooding time = 60 sec) | 43 |
| Figure 55: Von-Mises stress contour at the time of cooling down to 400 K (power = 45 kW/m, flooding time = 60 sec)..... | 43 |
| Figure 56: Core power in REA at HFP condition..... | 44 |
| Figure 57: Axial power shape used in the REA HFP case | 45 |
| Figure 58: Coolant temperature calculated using BISON | 45 |
| Figure 59: Fuel temperature change during an REA at HFP condition..... | 45 |
| Figure 60: Temperature distribution at the time of peak fuel temperature | 46 |
| Figure 61: Cladding surface output heat flux in comparison to critical heat flux | 46 |
| Figure 62: Cladding von-Mises stresses (rod-to-rod contact)..... | 46 |
| Figure 63: Cladding von-Mises stresses (no constraints) | 47 |
| Figure 64: Cladding von-Mises stress contours at the time of peak fuel temperature..... | 47 |
| Figure 65: Cladding stresses at the valley location..... | 47 |
| Figure 66: Cladding hoop and axial strains at the valley location..... | 48 |
| Figure 67: Rod linear power in a control rod ejection accident..... | 48 |
| Figure 68: Coolant temperature calculated by BISON code | 49 |
| Figure 69: Peak fuel temperature during the REA at HZP | 49 |
| Figure 70: Cladding temperatures at the valley and tip during the REA at HZP | 49 |
| Figure 71: Heat flux at the cladding valley and tip in comparison to the critical heat flux..... | 50 |
| Figure 72: Cladding von-Mises stress at the valley and tip locations during the REA at HZP condition with rod-to-rod contact | 50 |
| Figure 73: Cladding von-Mises stress at the valley and tip locations during the REA at HZP condition without rod-to-rod contact | 50 |
| Figure 74: Cladding stress components at the valley location without rod-to-rod contact | 51 |
| Figure 75: Cladding hoop and axial strains at the valley location..... | 51 |

LIST OF TABLES

| | |
|--|----|
| Table 1: Design characteristics for Lightbridge metallic fuel | 3 |
| Table 2: List of material property/behavior models developed for BISON | 5 |
| Table 3: Measured thermal conductivity of U-50 wt% Zr..... | 6 |
| Table 4: Comparison between measurement data to models..... | 10 |
| Table 5: Measured creep rate of U-Zr alloy [5]..... | 11 |
| Table 6: Mean coefficient of thermal expansion of U-Zr alloy [6] | 16 |
| Table 7: Coolant channel input parameters | 30 |
| Table 8: Fuel dimensional changes at EOL | 34 |
| Table 9: Input variables on modeling the thermal hydraulics boundary conditions..... | 40 |
| Table 10: Input parameters for the UO ₂ fuel case..... | 40 |
| Table 11: Comparison of peak cladding temperature between UO ₂ fuel and UZr ₂ fuel | 43 |

1. INTRODUCTION

The nuclear industry wishes to enhance accident tolerance and improve fuel utilization of Light Water Reactors (LWRs). This could be achieved by innovative fuel designs. One proposed fuel concept is the use of metallic fuel in LWRs.

The use of metallic fuel in water cooled reactors can be dated back to 1950s. The most common form is uranium alloyed with other elements, and many of the reports found in our literature review are from those early studies [1-6]. Since then, ceramic uranium dioxide materials became the dominant fuel type. In research and marine reactors, the operating experience of metal fuel in water reactors does exist [7][8], but no metallic fuel has been used in commercial reactors.

Metallic fuel has its technical merits: its high thermal conductivity allows low operating temperatures and enhanced safety in accident conditions. With appropriate fuel designs, little modification would be needed for its deployment in existing reactors. The Fukushima accident has further prompted the consideration of metallic fuels for use in LWRs to improve their accident tolerance [9]. With current challenges and known issues of the ceramic fuel, particularly fuel performance issues at high burnup conditions, it would be worthwhile to evaluate the metal fuel to assess the technical and economic feasibility as an alternative fuel for LWRs.

Despite the existence of many studies of metal fuel in fast reactors, the study of metal fuel in LWR is very limited. At present, there is one public company, Lightbridge Corp., that has been pursuing metallic fuel development for commercial applications in LWRs. Fuel design and fabrications are still in the early stage. Experimental programs in the US have just started, and it may take a long time to accumulate sufficient data for fuel qualification, and even longer for operation issues to emerge. In addition to those technical challenges, significant regulatory hurdles remain in the use of metallic fuel in LWRs. The current regulations for the fuel, for example Standard Review Plan (SRP) Chapter 4.2 [10], solely deals with ceramic UO_2 fuel and zirconium alloy cladding and is not adequate to address issues with metallic fuel proposed for use in LWRs.

It is of interest to develop an analytical capability of modeling metal fuel to examine fuel response and develop fuel performance metrics. This would enable utility customers and nuclear regulators to perform fuel qualification and licensing evaluations, should the needs arise. Current endeavor leverages the modeling and simulation capabilities developed in U.S. DOE's Nuclear Energy Advanced Modeling and Simulation (NEAMS) program, in particular, uses the BISON fuel performance code developed at Idaho National Laboratory (INL) as the analytical tool for modeling metal fuel behavior in LWRs.

The common form of metallic fuel is uranium alloyed with other elements, among which, the U-Pu-Zr and U-Zr alloys have been mostly used as fuel materials in fast reactors. In LWR conditions, there is little information available to ascertain a dominant fuel material. Therefore, in current study, we focus on the fuel design proposed by Lightbridge Corp. Material and geometric information of the fuel design were based on several patents, papers, and presentations [11-17].

Figure 1 shows important features of the design. The fuel rod design features a multi-lobe geometry with a helical twist along the axial direction. The fuel rod cross-section consists of a fuel core, displacer, and a barrier (cladding) to prevent the release of fission products.

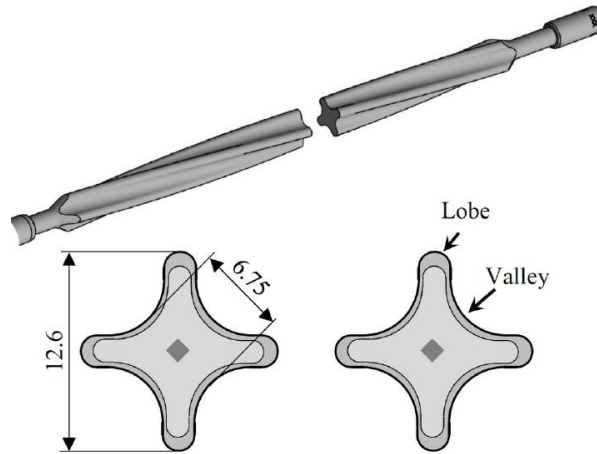


Figure 1: Schematic of Lightbridge metallic fuel design [11]

The fuel material is δ -phase U-Zr₂. The cladding material is a Zr-Nb alloy, and the displacer is a Zirconium alloy. The cladding is metallurgically bonded to the fuel core, therefore there is no free volume (gap or plenum) in the fuel rod.

References [13-15] indicate that the number of lobes could vary to fit the geometric shape of the assembly. The four-lobe design, which fits a square assembly, is more commonly seen in the literature, while the three-lobe design, which fits a hexagonal assembly, also appears in some references. According to Ref. [17], this fuel design is based on fuels previously used in Russian icebreaker reactors, however, no original design information for the fuel used in icebreaker reactors is found in our open literature survey. We found reference to a helical fuel design with three lobes (in a cross-sectional view) possibly used in submarine reactors [7]. A similar four-lobe fuel design with a helical cruciform geometry was also used in the fuel design in a research reactor [18]. It should be noted that the helical geometry fuel has been studied for ceramic fuel for both PWR and BWRs on its thermal hydraulics, although the cross-sectional geometry differs from the Lightbridge fuel design [19-21].

From fuel performance perspective, the number of lobes in the fuel design is not a significant variable, and this project will only study the four-lobe geometry, which is compatible with the square geometry of PWR assemblies. Additionally, more information is available for this design. For the four-lobe design, the range of design parameters that describes the geometry is reported in Ref. [13].

The fuel design allows each fuel element to touch the surrounding fuel elements at certain heights along the fuel length (these are called self-spacing planes), which occur every $\frac{1}{4}$ length of the twist pitch (i.e., the length along the fuel rod axis for every 360-degree twist). Between each set of adjacent self-spacing planes, the open channel allows the flow mixing. The pitch of axial twist is between 5% and 20% of the length of the fuel element [13, 14]. The number of the self-spacing planes along the fuel rod length is:

$$N = n * L / h \quad (\text{Eq. 1})$$

Where, L is fuel rod length, n is the number of lobes and h is the twist pitch.

Table 1 lists the design characteristics range and one set of example parameters. Figure 2, taken from a patent filed by Lightbridge Corp. [13], shows a cross section view of the metallic fuel with annotated geometry parameters.

Table 1: Design characteristics for Lightbridge metallic fuel

| Symbol* | Unit | Characteristic | Range | Example |
|-----------------|-----------------|--|---------------------------|---------|
| D | mm | Major Diameter Across Lobes | 9 – 14 | 12.6 |
| Δ | mm | Thickness of Lobes | 2.5 – 3.8 | 3.06 |
| r | mm | Outer Radius of Cladding at Lobe | $\Delta/2$, $\Delta/1.9$ | 1.53 |
| r_f | mm | Inner Radius of Cladding at Lobe | 0.5 – 2.0 | 1.2 |
| δ_{\max} | mm | Thickness of Cladding at Ends of Lobes | 0.4-2.2 | 1.02 |
| δ | mm | Thickness of Cladding at Valleys | 0.4 – 1.2 | 0.40 |
| R | mm | Radius Defining Outer Curvature at Valleys | 2 - 5 | 2.97 |
| a | mm | Displacer Width (i.e., Side Length) | 1.5 – 3.5 | 1.56 |
| | mm | Fuel Element Perimeter | 25 - 60 | 40.16 |
| | mm ² | Fuel Core Area | 30 – 70 | 37.49 |

*Symbols are shown in Figure 2.

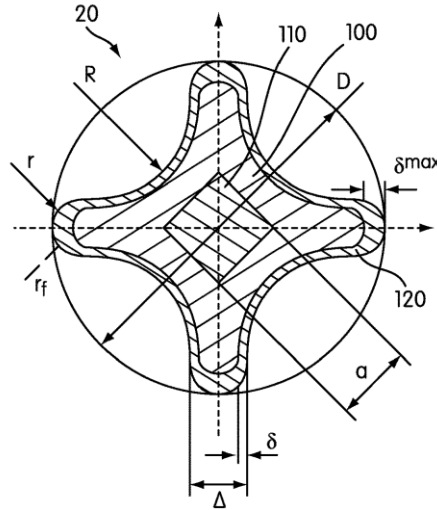
**FIG. 9****Figure 2: Cross section view of Lightbridge metallic fuel design [13]**

Table 1 is used in the BISON modeling for creating the finite element grid and input geometry parameters. Appendix A provides a script that is used to compute geometry parameters for this fuel design.

The metallic fuel design by Lightbridge for LWR application uses δ -phase U-Zr alloy which has different material properties than what is typically used for fast reactor fuel. Material models in the BISON code were mainly developed for fast reactor fuel modeling purpose, and they may not be applicable for the δ -phase U-Zr. New material and behavioral models have been developed and implemented in BISON to provide the capabilities for the performance evaluation of metal fuel under normal operation and accident scenarios in an LWR environment.

The report is organized as follows.

Section 2 summarizes all new material models that are developed or adopted from literature for δ -phase U-Zr alloy, and cladding corrosion and coolant channel model modifications for modeling this fuel design described in above sub-section.

Section 3 describes finite element modeling method, BISON code modifications, and some assumptions made in the modeling approach.

Section 4 describes the results for modeling a metal fuel rod in normal operation and discusses the figures of merits for metal fuel.

Section 5 provides results for transient and accident modeling and discusses the possible failure mechanisms.

Section 6 provides a summary of this report and recommendations for future studies.

2. MATERIAL MODEL DEVELOPMENT

2.1 U-Zr Material Models

This section provides a description of the material models developed and implemented in BISON for modeling Lightbridge metal fuel, which includes the data basis, sources, applicable range, and comparison to other material models, if applicable.

We performed a review of the material property data in the open literature [5][6][22-34], and developed and/or adopted material models for implementation in the BISON code. These new models are listed in Table 2. Section 2.1.1 – 2.1.9 describes models for UZr_2 fuel material in detail. Appendix B shows these new material models in the materials block in BISON code input.

Table 2: List of material property/behavior models developed for BISON

| | Material Properties/Behavior | New Models Implemented in BISON* | Description |
|---|---------------------------------------|---|--|
| 1 | Thermal conductivity Specific heat | UZrThermal | Model to compute thermal conductivity and specific heat of δ -phase UZr. |
| 2 | Elastic modulus | UZrElasticityTensor | Model to compute elastic modulus of δ -phase UZr. Assumptions are made for the transition to γ phase |
| 3 | Deviatoric creep | UZrCreepUpdate | Model to compute creep of U-Zr alloy. A new model is developed using data in Ref. [5]. Due to the scarcity of data, $\alpha+\delta$ phase data is also used. |
| 4 | Thermal expansion | UZrThermalExpansionEigens train | An isotropic thermal expansion model for UZr_2 |
| 5 | Density | -- | Constant input of δ -phase U-Zr density at room temperature, which is 9870 kg/m^3 |
| 6 | Swelling | UZrVolumetricSwellingEigen strain | Model to compute solid and gaseous swelling of δ -phase U-Zr |
| 7 | Instantaneous plasticity | UZrPlasticityUpdate | Model to compute yield strength of δ -phase U-Zr |

**Those are names in newly created files for material models following the same naming convention used in BISON*

2.1.1 Thermal Conductivity

The measured thermal conductivity of U-Zr alloy at different temperatures for various compositions is shown in Figure 3. The data at 50 wt% Zr is digitalized from Figure 3 and shown in Table 3. Using this information, a polynomial fit of the measurement data is obtained and shown as Eq. 1.

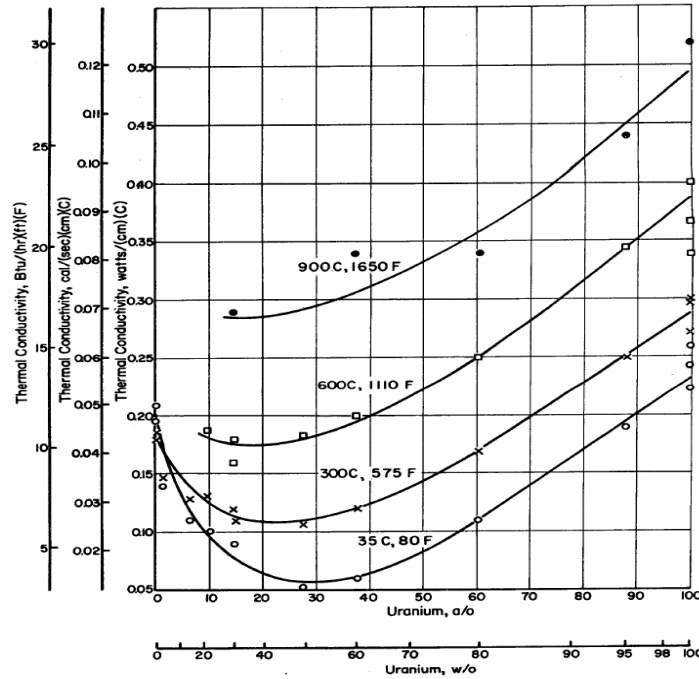


Figure 3: Measured thermal conductivity of U-Zr alloy [5]

Table 3: Measured thermal conductivity of U-50 wt% Zr

| at% U | T (°C) | T (K) | Thermal Conductivity (W/m-K) |
|-------|-----------|----------|------------------------------------|
| 27.4 | 35 | 308 | 5.23 |
| 27.7 | 300 | 573 | 10.51 |
| 27.4 | 600 | 873 | 18.30 |
| 26.4 | 900 | 1173 | 29.04 |

The resultant equation is:

$$k = 1.80 + 7.08 \times 10^{-3}T + 1.37 \times 10^{-5}T^2 \quad (\text{Eq. 1})$$

A comparison between the numerical fit (Eq. 1) and the Billone model in BISON [35] is shown in Figure 4. The difference is not significant, but appreciable, and more so in the operating temperature range of the Lightbridge-designed metallic fuel.

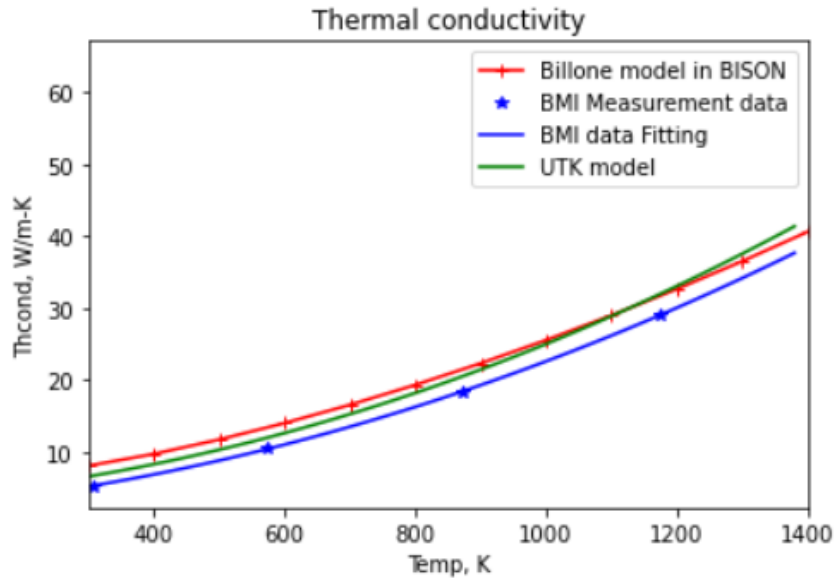


Figure 4: Comparison between thermal conductivity models of UZr₂

A thermal conductivity model has been developed by UTK, based on weighted average of data obtained from the INL metal fuels handbook [22] for U-64 at% Zr [24] and U-72 at% Zr [25]. The thermal conductivity fit to the fresh fuel was performed, assuming a similar polynomial expansion to temperature, and then prescribed with a non-dimensional density dependence, to account for thermal conductivity degradation due to burnup. The resulting recommended thermal conductivity model is given by:

$$k \left(\frac{\text{W}}{\text{m-K}} \right) = \frac{(3.29 + 6.2 \times 10^{-3}T + 1.55 \times 10^{-5}T^2) \times \rho(\text{burnup})}{\rho_0} \quad (\text{Eq. 2})$$

Where ρ is the density of metal fuel and subscript 0 represents the initial value. This model is compared with the simple fitting and Billone model as a validation (as shown in Figure 4), and is used as the default model for the analysis in Section 4 and 5.

Figure 5 is the temperature contour using the UTK model implemented in BISON code for a case with a linear power of 58 kW/m and an inlet temperature of 300°C. The peak fuel temperature is slightly lower than the result by Lightbridge in a similar input condition [17].

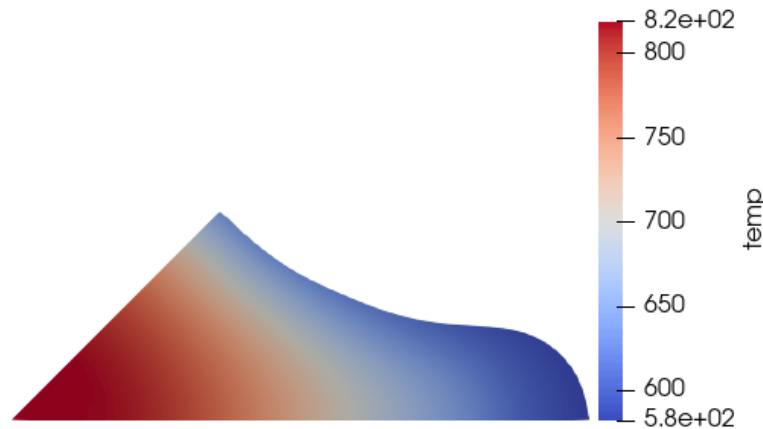


Figure 5: Fuel temperature prediction using UTK model in BISON

2.1.2 Heat Capacity

A specific heat model (in units of J/kg-K) was developed by UTK, in a similar manner as the thermal conductivity data. Data obtained from the INL metal fuels handbook [22] for U-Zr alloys containing between 63 and 72 at% Zr [26-28] were used to base the functional form of the fit, which is provided in Eq. (3):

$$C_p = 94.58 + 0.22T + 3.92 \times \frac{10^6}{T^2} \quad (J \, kg^{-1} K^{-1}) \quad (\text{Eq. 3})$$

A value of 140.93 gram/mol is used for UZr_2 (assuming ~18% U-235). The specific heat model for the δ -phase U-Zr alloy in Ref. [28] (shown in Eq. 4) was also implemented in BISON code for comparison.

$$C_p = 3.08 + 8.43 \times 10^{-3}T + 9.83 \times \frac{10^4}{T^2} \quad \left(\frac{\text{cal}}{\text{mol-K}} \right) \quad (\text{Eq. 4})$$

These two models tend to agree well, and the “Savage” model in BISON [35], for fast reactor U-Pu-Zr fuel, appears to underpredict the specific heat.

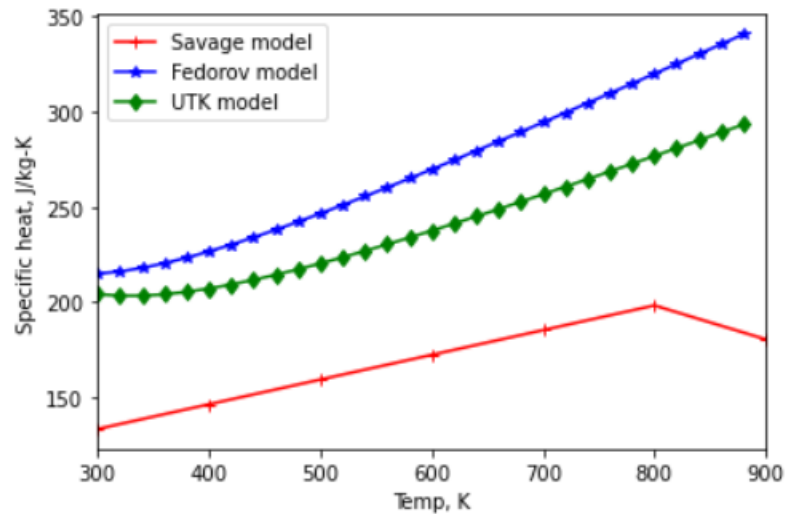


Figure 6: Comparison between different specific heat models for modeling UZr_2 alloy

In addition, a numeric integration over temperature using measured specific heat data in Ref. [29] is performed, and the resultant enthalpy versus temperature is shown in Figure 7 below.

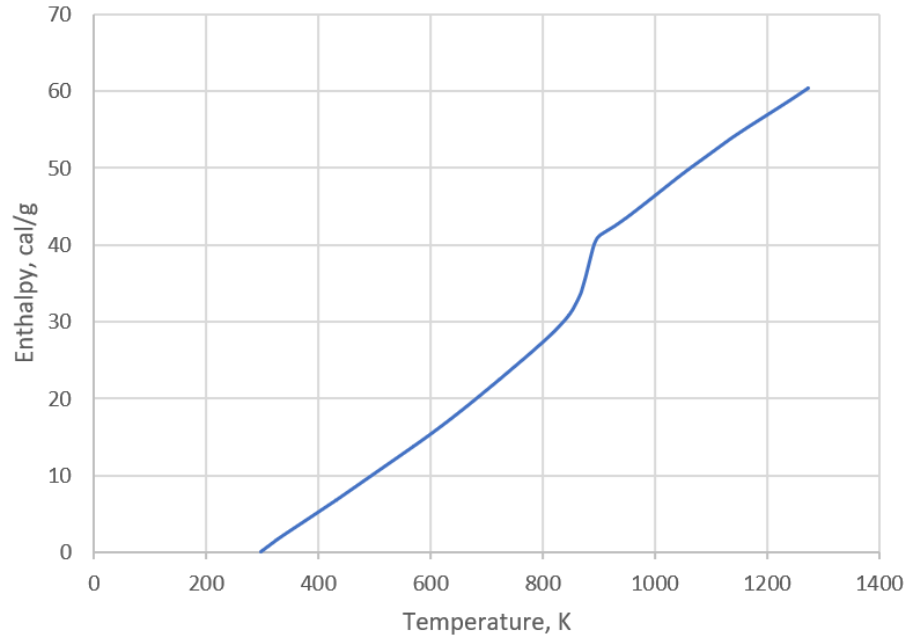


Figure 7: Enthalpy of UZr₂ versus temperature

2.1.3 Creep

Creep tests on U-50 wt% Zr alloy were reported by Kutty et al. [30]. In the study performed by Kutty et al., the creep test was performed using impression test. The temperature ranges from 525 to 575°C. The stress ranges from 13 to 37 MPa. The average activation energy was given as 106 kJ/mol [30]. Using the creep measurement data in Ref. [30], a fit was performed, and the result is shown in Figure 8.

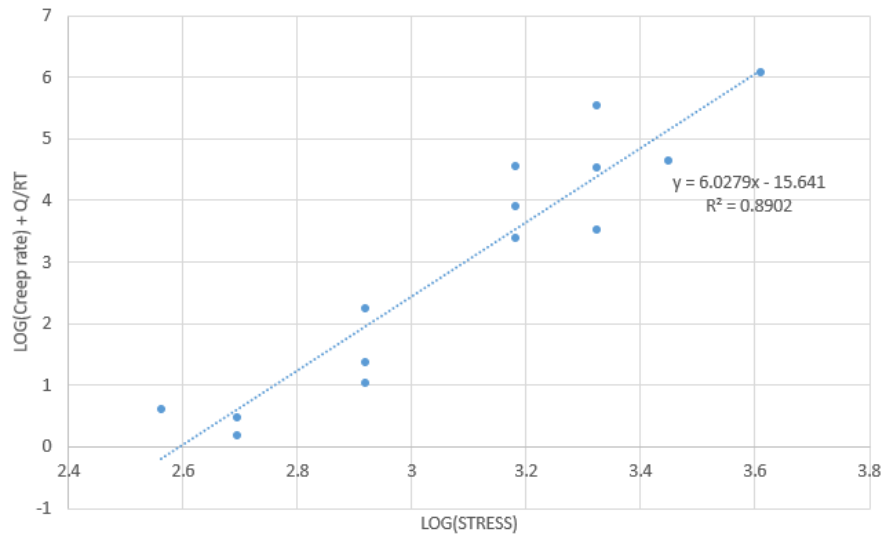


Figure 8: Fitting measured data of UZr₂ to a power-law creep model

The resultant power-law creep equation is:

$$\dot{\epsilon} = A \exp\left(-\frac{Q}{RT}\right) \sigma^n \quad (\text{Eq. 5})$$

Where, $A = 1.611\text{E-}7$, $Q = 106 \text{ kJ/mol}$, $n = 6.0279$, $R = 8.314 \text{ J/mol-K}$, T is temperature in Kelvin, and σ is stress in MPa.

The measurement data is only for a very limited temperature range, and an extrapolation of the model to a wider temperature range is plotted against the reciprocal of temperature at a stress of 35 MPa as shown in Figure 9. The current BISON model (including both diffusional and dislocation creep models) for fast reactor U-Pu-Zr fuel and the Limbäck creep model for Zry are also plotted for comparison. The Kutty model predicts the creep rate a few orders of magnitude higher than the model predictions for U-Zr alloy and Zry in BISON.

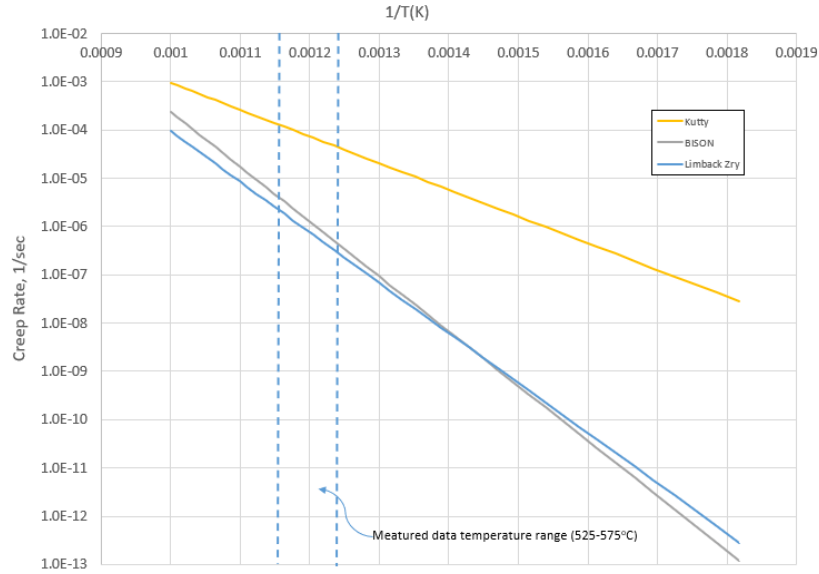


Figure 9: Comparison between Kutty model and BISON models at 35 MPa

Ref. [5] has the measured creep rate data for the U-60 wt% Zr alloy. At 450°C, the measured creep rates at three different stresses were also compared to model predictions and results are shown in Table 4. None of those models seem to match the measurement data.

Table 4: Comparison between measurement data to models

| Composition (wt% Zr) | Temperature °C | Stress MPa | Creep Rate | | Kutty Model 1/sec | BISON (dislocation creep) 1/sec |
|-------------------------|-------------------|---------------|------------|----------|-------------------------|--|
| | | | 1/hr | 1/sec | | |
| 60 | 450 | 137.9 | 1.00E-05 | 2.78E-09 | 2.79E-02 | 4.85E-06 |
| 60 | 450 | 72.4 | 1.00E-06 | 2.78E-10 | 5.74E-04 | 2.67E-07 |
| 60 | 450 | 68.9 | 8.00E-07 | 2.22E-10 | 4.28E-04 | 2.15E-07 |

Since the creep measurement data for δ -phase U-Zr alloy is very limited, we expanded the data to include higher zirconium alloy ($> 60 \text{ wt\% Zr}$) for the creep model development. The resultant power law model is shown in Figure 10 and in Eq. 6.

$$\dot{\epsilon} = A \exp\left(-\frac{Q}{RT}\right) \sigma^n \quad (\text{Eq. 6})$$

where, $A = 0.0041328$, $Q=210$ kJ/mol, $n = 4.4715$, $R=8.314$ J/mol-K, T is temperature (K), and σ is stress (MPa).

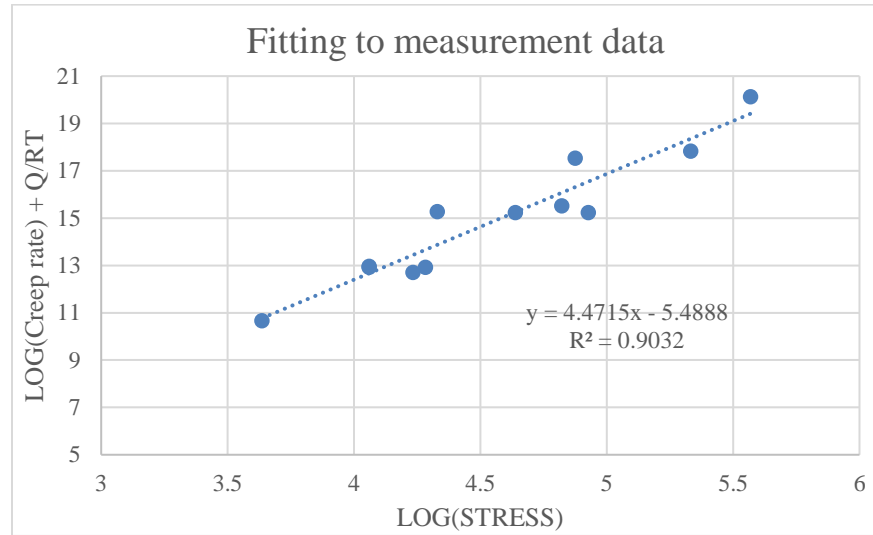


Figure 10: Fitting measured creep rate of UZr₂ alloy to a power-law creep model

The creep rate data reported in Ref. [5] is listed in Table 5. The measurement data in the temperature range of 400 – 500°C are used for the fitting in Eq. 6).

Table 5: Measured creep rate of U-Zr alloy [5]

| Zr wt% | Temperature °C | Stress MPa | Creep Rate 1/sec |
|--------|----------------|------------|------------------|
| 59 | 450 | 137.9 | 2.78E-09 |
| 59 | 450 | 72.4 | 2.78E-10 |
| 59 | 450 | 69.0 | 2.22E-10 |
| 78 | 400 | 262.0 | 2.78E-08 |
| 78 | 400 | 206.8 | 2.78E-09 |
| 78 | 400 | 124.1 | 2.78E-10 |
| 78 | 450 | 131.0 | 2.78E-08 |
| 78 | 450 | 103.4 | 2.78E-09 |
| 78 | 450 | 57.9 | 2.78E-10 |
| 78 | 500 | 75.8 | 2.78E-08 |
| 78 | 500 | 57.9 | 2.78E-09 |
| 78 | 500 | 37.9 | 2.78E-10 |
| 72.6 | 815 | 3.4 | 6.94E-08 |
| 47.1 | 815 | 3.4 | 4.96E-08 |
| 72.3 | 980 | 3.4 | 4.87E-06 |
| 63.7 | 980 | 3.4 | 5.56E-06 |
| 47.1 | 980 | 3.4 | 1.74E-05 |

To use the creep model in the entire operation temperature range, a transition between the δ phase and γ phase is modeled using a smoothing function. The γ phase model in BISON remains same, which is:

$$\dot{\epsilon}_{dislocation}^{\gamma} = 0.08 \left(1 - p^{2/3}\right)^{-3} \exp\left(\frac{-28500}{RT}\right) \sigma^3 \quad (\text{Eq. 7})$$

where, p is porosity, T is temperature (K), σ is von-Mises stress (MPa) and $R = 1.987$ cal/mol-K [35]. The phase transition temperatures used in the model are described in 2.1.6.

2.1.4 Density

A recommended value of 9.87 g/cm^3 as the density of $\delta\text{-UZr}_2$ is shown in Ref. [22]. This represents an intermediate composition (70.7 at% Zr), and the density was calculated using lattice parameters measured from high-resolution neutron-diffraction data. As-cast U-Zr alloy shows slightly lower density, and at 50 wt% Zr, the density is $\sim 9.54 \text{ g/cm}^3$. The lower density was attributed to flaws such as porosities and impurities [22]. Without information on the as-fabricated porosities, we used 9.87 g/cm^3 exclusively in the analysis.

2.1.5 Elastic Modulus

The elastic modulus E (GPa) in the δ -phase is a linear fitting to the reported data on arc-melted and induction-melted samples at different temperatures in Ref. [6]. The equation for the elastic modulus is a function of temperature T (K):

$$E = -0.0492 T + 144.46 \quad (\text{Eq. 8})$$

The applicable temperature range is 295 K - 753 K.

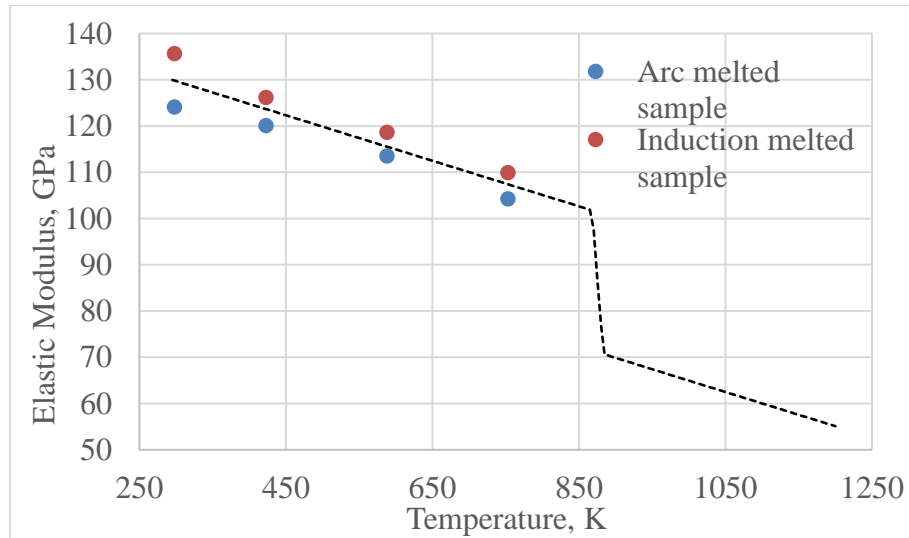


Figure 11: Elastic modulus of UZr_2 as a function of temperature

There is no data available above the phase transition temperature. A reduction of modulus is expected, and the same reduction factor used for the U-Pu-Zr alloy model in BISON is used. This gives a 30% reduction of modulus in the gamma phase. Plot of elastic modulus versus temperature in comparison with measurement data is shown in Figure 11. The induction melted sample has a higher modulus than arc melted sample, and this was attributed to possible contamination with

impurities such as carbon or oxygen [6]. Fedorov et al. measured the elastic modulus of U-Zr alloy at 295 K, and the elastic modulus decreases with the increase of weight fraction of Zr [22]. Their measurement for δ phase U-Zr at room temperature is slightly higher than the prediction in Eq. 8.

A constant Poisson's ratio of 0.32 is used based on the calculation using current BISON model for U-Pu-Zr alloy.

2.1.6 Phase Transition

The δ -phase is a stable phase in binary U-Zr alloys, and its compositional range can be affected by impurities such as oxygen and nitrogen. For low concentrations of O and N, the minimum concentration of Zr is 43 wt% at 500-550°C, and 40.5–40.7 wt% at 600°C; the maximum concentration of Zr is 59 wt% [22].

For the phase transition (from δ to γ phase) in many of the material models, it is necessary to have a smooth transition as a function of temperature. Therefore, a phase transition start temperature and end temperature are needed. Based on the phase diagram shown in Figure 12, at the composition close to 50 wt% Zr, temperature from 868 K to 883 K are used in material models for the phase transition. Note that the δ phase is called ϵ phase as shown in Figure 12 in early studies.

In addition, there are two models (named as PhaseUPuZr and ADUPuZrLookup) in the BISON code that can be used to compute the phase using temperature and composition of the U-Pu-Zr alloy. The binary U-Zr alloy is bounded by the above models. Those models could also be used to determine the transition temperatures.

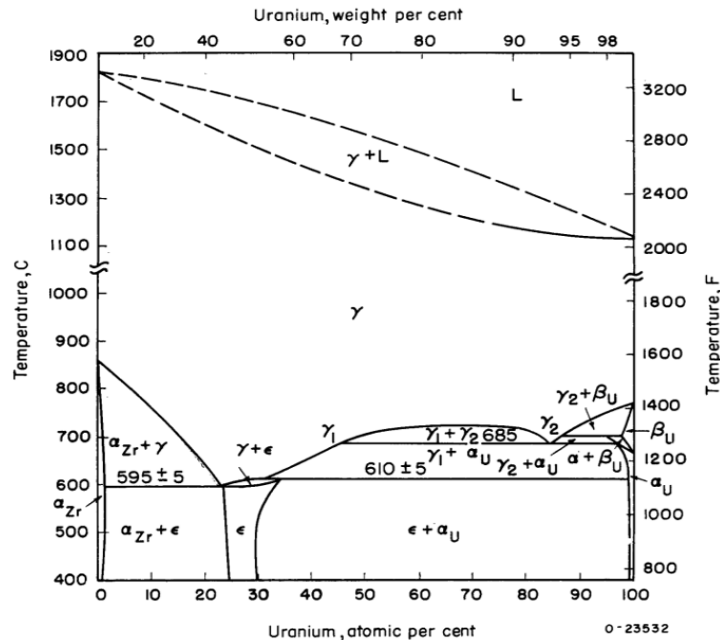


Figure 12: Zirconium-uranium phase diagram [6]

2.1.7 Yield Strength

Figure 13– Figure 15 are created using data summarized in Ref. [6] on the mechanical test data for U-Zr alloy with added trend lines. The ultimate tensile strength and yield strength of U-Zr alloy at

room temperature is shown in Figure 13. The yield strength at 370°C is shown in Figure 14. The uniform elongation at room temperature is plotted in Figure 14. For δ -phase, the strength is relatively higher, but the ductility is lower as compared to the α -phase U-Zr alloy used as fast reactor fuel element.

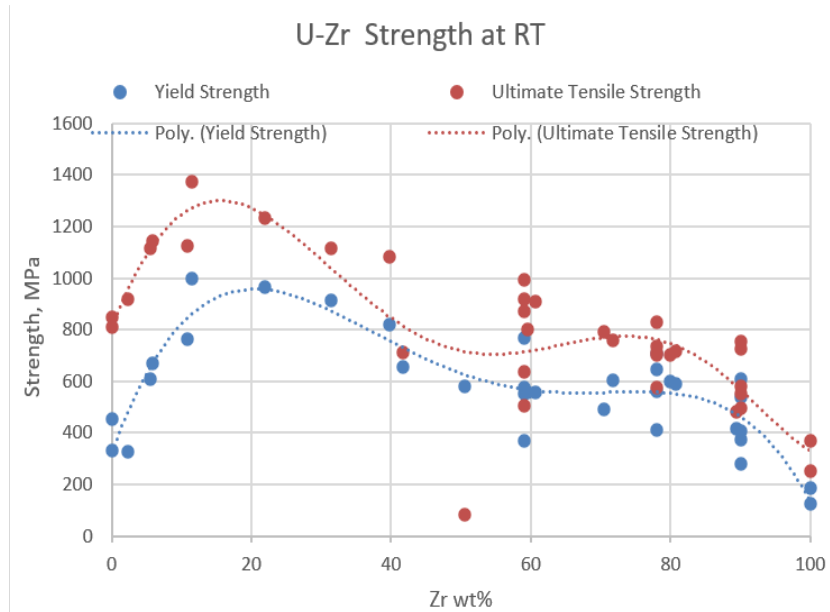


Figure 13: Ultimate tensile strength and yield strength of U-Zr alloy at room temperature

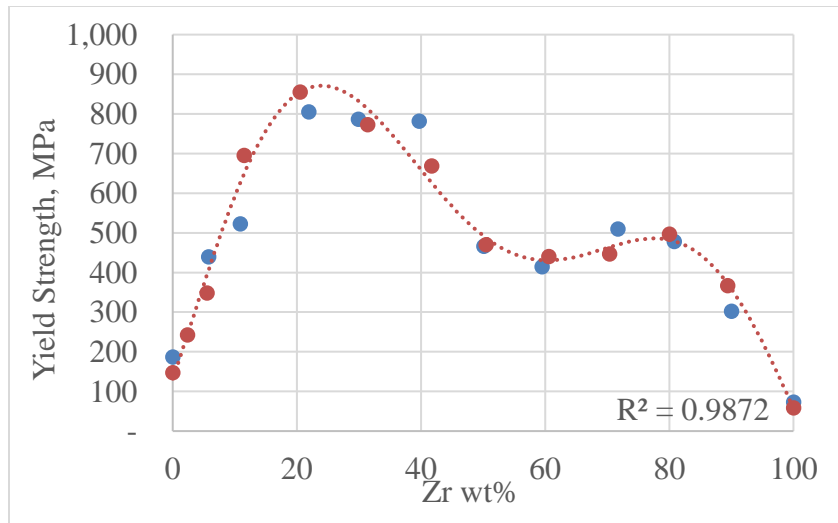
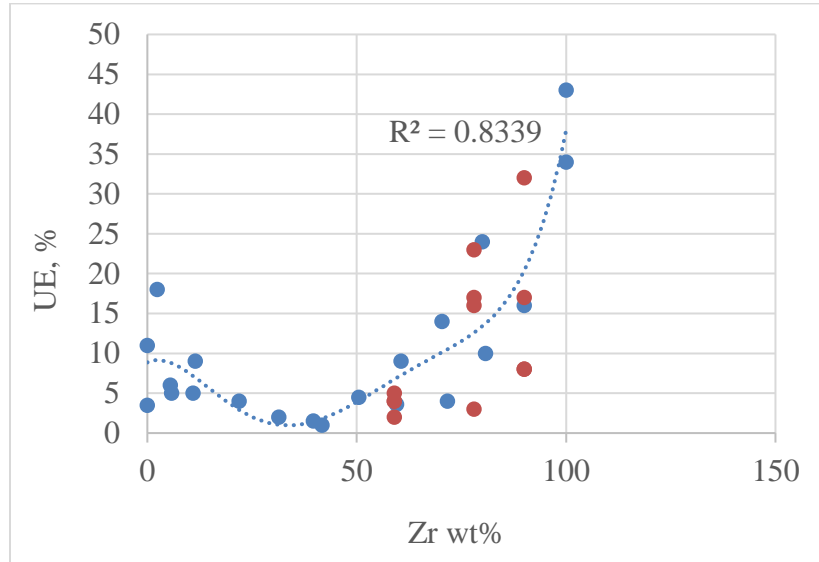


Figure 14: Yield strength of U-Zr alloy at 370°C

The yield strength decreases when temperature increases. The yield strength for δ -phase U-Zr at room temperature is ~ 600 MPa, and it is reduced to ~ 500 MPa at the temperature of 370°C. No measurement data on mechanical strength is available to develop a model for high temperatures. The measured hardness data from Ref. [5] shown in Figure 16 indicates the significant reduction of the strength of the δ -phase U-Zr at elevated temperatures. Assuming the measured hardness is proportional to the yield strength, the yield strength at higher temperatures can be inferred from the hardness measurements. A comparison of the yield strength between UZr_2 and MATPRO model for Zircaloy

[36] is shown in Figure 17. It appears that applying a multiplier of 1.4 to the Zry model can provide a good lower bound of yield strength for U-Zr alloy in the operation temperature range in the δ -phase. In the γ phase, the yield strength of UZr_2 might be close to the model of Zry. Therefore, we used the MATRPO Zry model with a multiplier for the estimation of the yield strength of UZr_2 in the analysis. Since later studies have shown that the fuel yield strength (from this estimation) is well above the maximum effective stresses in fuel core, no further refinement of this model has been made.



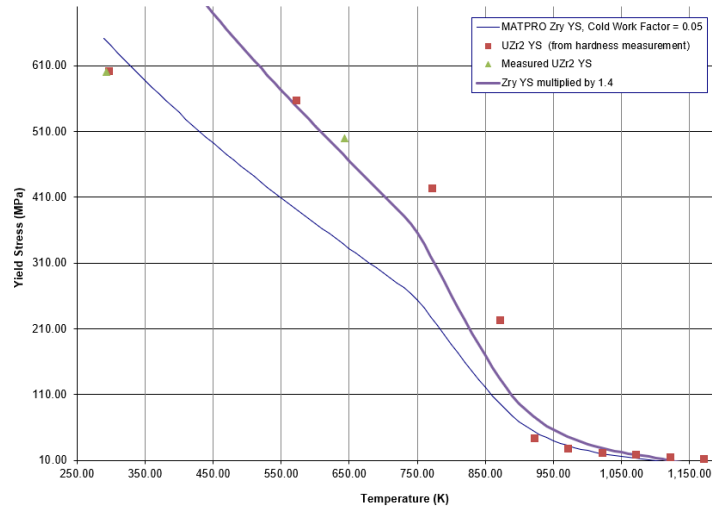


Figure 17: Comparison of yield strength between UZr₂ and MATPRO Zry model

2.1.8 Thermal Expansion

An isotropic thermal expansion model is developed using data in Ref. [6] on the U-50 wt% Zr alloy. The equation for the linear thermal expansion strain is:

$$\frac{\Delta L}{L} \% = \begin{cases} 4.0 \times 10^{-7} T^2 + 7.68 \times 10^{-4} T - 0.020759 & T \leq 615^\circ \text{C} \\ 6.76 \times 10^{-3} T - 3.5551 & 615^\circ \text{C} < T \leq 631^\circ \text{C} \\ 1.445 \times 10^{-3} T - 1.9859 \times 10^{-3} & T > 631^\circ \text{C} \end{cases} \quad (\text{Eq. 9})$$

where T is temperature in °C. The applicable temperature range is 20 to 1000°C.

Mean coefficient of thermal expansion (CTE) of δ -phase U-Zr alloy measured at different temperature ranges for two types of test specimens with different heat treatments and compositions (60 wt% and 50 wt% Zr), are also provided in Ref. [6] as reproduced in the following table. In δ -phase, there is a small variation in the mean CTE for different test specimens, and all of them are consistently lower than that in γ phase.

Table 6: Mean coefficient of thermal expansion of U-Zr alloy [6]

| U, wt% | Temperature range (°C) | Mean CTE, 10^{-6} | Test Specimen |
|--------|------------------------|---------------------|----------------------------|
| 41 | 20-330 | 9.4 | Furnace cooled from 815°C |
| 41 | 20-550 | 10.2 | Furnace cooled from 815°C |
| 50 | 20-300 | 8.6 | Furnace cooled from 1000°C |
| 50 | 20-550 | 9.6 | Furnace cooled from 1000°C |
| 50 | 650-1000 | 14.1 | Furnace cooled from 1000°C |

The CTE for as-cast and heat treated (550°C for 24 hrs followed by quench) samples with composition of U-50 wt% Zr, U-60 wt% Zr, and U-70 wt% Zr were reported in [31]. In the temperature range of 30 to 600°C, the mean CTE is 4.24×10^{-6} (1/K) for heat treated U-50 wt% Zr. As-cast material, however, shows higher thermal expansion and unstable behaviors. The thermal expansion equation for heat-treated U-50 wt% Zr is:

30-600°C:

$$\frac{\Delta L}{L} \% = -0.00344 + 1.978 \times 10^{-4}T + 4.72704 \times 10^{-7}T^2 + 2.04694 \times 10^{-10}T^3 \quad (\text{Eq. 10})$$

650-1000°C:

$$\frac{\Delta L}{L} \% = 0.12321 + 1.15746 \times 10^{-4}T + 3.48886 \times 10^{-7}T^2 - 1.34308 \times 10^{-10}T^3 \quad (\text{Eq. 11})$$

A comparison of linear thermal expansion strain from References [31] and [6] and the model is shown in Figure 18. The fitting in Eq. 9) is close to the model for as-cast material in Ref. [31], but this may simply be a coincidence. The preferred grain orientation may also affect the thermal expansion, but no information of grain orientation is available to develop an anisotropic model. The model in Eq. 9) is used for the analysis since this appears to be bounding the data surveyed from literature.

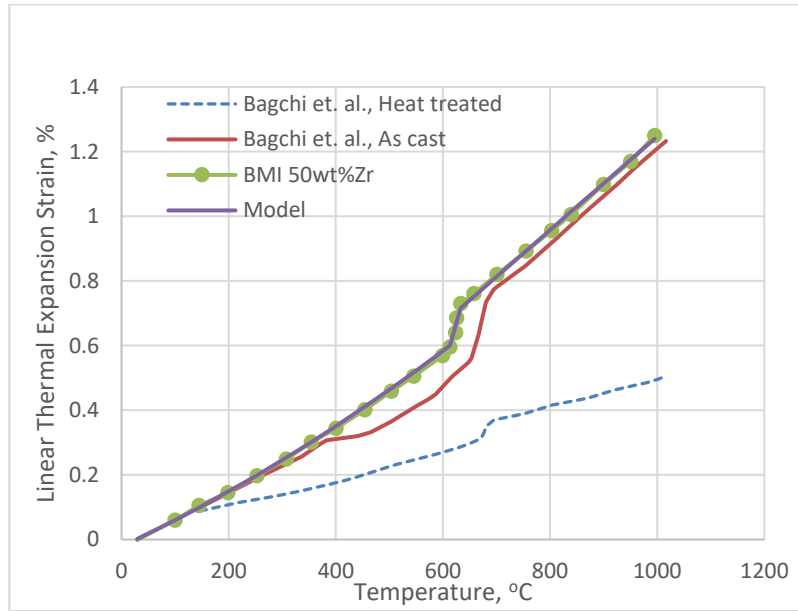


Figure 18: Linear thermal expansion strain versus temperature

2.1.9 Fuel Swelling

The volumetric strain due to solid fission product swelling in BISON for fast reactor U-Pu-Zr fuel is assumed to be proportional to burnup:

$$\varepsilon_s = C \cdot Bu \quad (\text{Eq. 12})$$

C is a constant with a typical value from 1.2% to 1.5% per 1% atomic burnup.

There is very limited data on the swelling rate of δ -phase U-Zr, most of those irradiation experiments were conducted at low burnups and low irradiation temperatures [6]. The fuel swelling for the δ -phase U-Zr might be similar to the high zirconium alloys [6]. It was estimated that the solid fission product swelling is 2 to 2.5% per 1% FIMA for the high zirconium alloy. At 425 – 428°C, the average fuel swelling is roughly 3% per 1% FIMA as shown in Figure 19 for the high zirconium alloy (78 wt%

Zr) [6]. According to [41], the swelling rate for δ -phase U-Zr fuel is 1% per 1%FIMA. This is close to 1.06% per 1% FIMA in a theoretical estimation assuming substitution in solid solution and elastic deformations around fission atoms [5]. In the literature, the low swelling rate was reported for less than 1% per 1% FIMA at 280°C with a low burnup of 1.75% FIMA [5]. Those data in [5][6] were reviewed, but there was no sufficient information to develop a new swelling model.

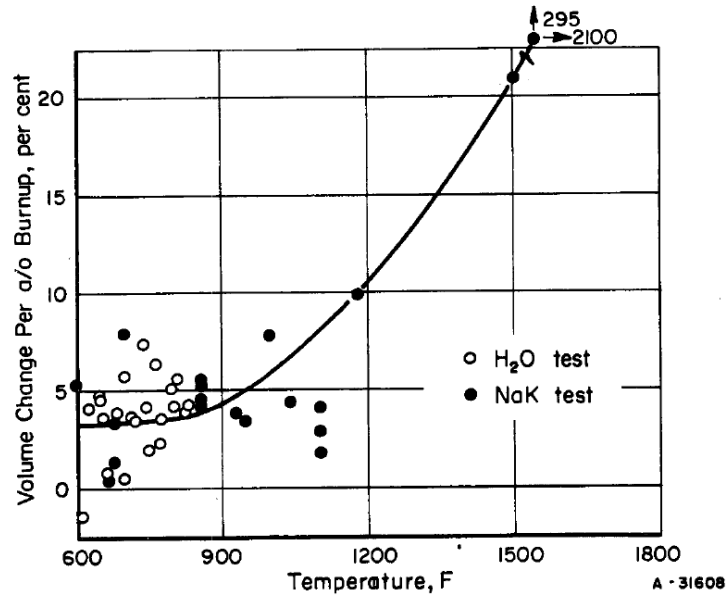


Figure 19: Volume change versus temperature for U-Zr alloys containing up to 22 wt% uranium [6]

Models implemented for computing the swelling of δ -phase U-Zr consists of a solid swelling model using 1.5% per 1% FIMA in Eq. 12), and a gaseous swelling model.

The gaseous swelling model was developed, with a number of key assumptions resulting from limited data in the literature for δ -phase U-Zr. In particular, we assessed the Xe diffusivity to be the result of a radiation-enhanced diffusion due to super-saturated point defect concentrations under irradiation, and assuming an activation energy of 1.6 eV. Due to the high electronic conductivity of δ -phase U-Zr, we have assumed no heterogeneous (electronic stopping) contribution to either the xenon diffusivity or to fission gas re-solution from intragranular fission gas bubbles. Based on the input from the initial BISON modeling, we have focused on fuel irradiation temperatures from ~360 to 600°C and grain sizes of either 10 or 130 microns. The resulting xenon diffusivity and δ -phase U-Zr physical properties were then modeled using the Nyx simplified fission gas diffusion and bubble formation model [42][43], which includes xenon intragranular bubble formation and xenon diffusion to the grain boundaries, using a range of xenon diffusivity values to assess the anticipated uncertainty in the point defect super-saturation. The results of the Nyx simulations were then used to populate an engineering scale model of fission gas bubble swelling.

It is important to note that, as a result of the predicted high xenon diffusivity and small grain sizes, the Nyx model indicated that xenon transport to the grain boundaries should dominate the fate of the xenon, relative to the formation of intragranular bubbles. Correspondingly, we have assumed an areal density of $5 \times 10^{11} \text{ m}^{-2}$ grain boundary bubbles, in order to assess the predicted fission gas swelling. Figure 20 and Figure 21 presents the resulting fission gas swelling model, and indicates significant predicted swelling that is dominated by the intergranular bubbles. It is also shown in these figures that the swelling strain for the large grain case is slightly lower than the small grain case.

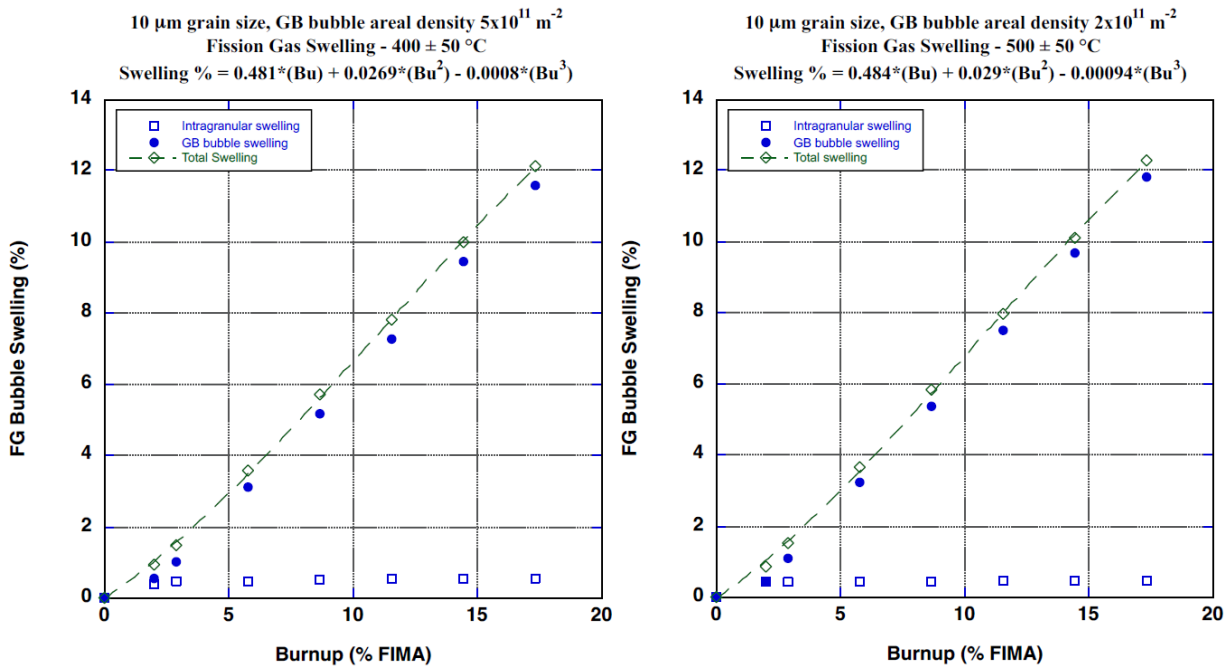


Figure 20: Model of gaseous swelling rate versus burnup for 10 μm grain size

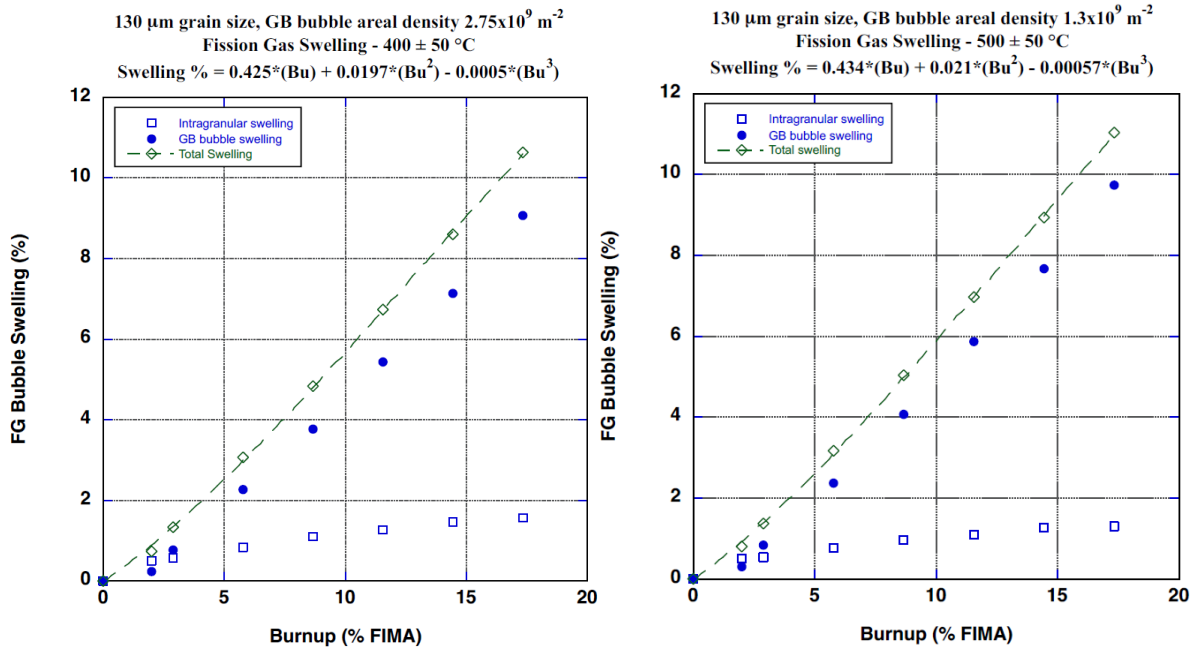


Figure 21: Model of gaseous swelling rate versus burnup for 130 μm grain size

In the operating temperature regime, the gaseous swelling model is insensitive to the temperature, and the fitting for the 10 μm grain size at 400°C is used as the default model in the analysis. That would give a total fuel swelling rate of 2-3% per 1% FIMA, slightly lower than the swelling of high zirconium alloy in Ref. [6].

2.2 Zr-Nb Cladding Alloy Models

The Lightbridge fuel design uses Zr-Nb alloy as cladding material, although no specific information is provided on the details of the composition, heat treatment etc. We turned to searching information on a few types of Zr-Nb alloys used as cladding material including ZirloTM, M5TM, and E110 (Zr-

1%Nb used for VVER fuel). Some thermal and mechanical material properties are found in the literature [37][38] for Zr-1%Nb cladding alloy, but the difference between Zr-4 and those Zr-Nb material is small, and current models for Zr-2 and Zr-4 used in BISON code are deemed adequate, the generic material models for Zr-4 implemented in BISON code would be used for modeling the metal fuel.

The burst strength of Zr-1%Nb reported in the literature appears to be lower than Zr-4. This could affect the ballooning and burst of cylindrical fuel pin clad with zirconium alloy metal, but this fuel design rules out the mechanisms of ballooning and burst, and therefore the burst failure model is not implemented.

Literature data has shown that the presence of Nb in general improves the corrosion resistance of Zirconium alloy. Those models for Zr-4 in BISON could over-estimate the oxide layer thickness and hydrogen uptake as compared to Zr-Nb cladding alloy. The corrosion models for the M5TM material in Ref. [44][45] were adopted for the modification of BISON code for the modeling work.

One main concern on the burnup extension of current LWR fuels is the water-side corrosion and hydrogen pickup, which would reduce the cladding ductility, and in accident conditions, the fuel would be more prone to failure. The corrosion and hydride precipitate in the cladding wall would still exist in this metallic fuel design with Zr-Nb cladding. Although to quantify the effect of material degradation to the fuel failure is less clear at present, it is important to model this phenomenon to provide insights for this fuel design. Those corrosion models in BISON and in literature are examined in detail. A few corrosion models for Zr-4 cladding in normal operation conditions of PWRs are currently implemented in BISON code. The corrosion modeling in BISON code uses the correlation which consists of a pre-transition stage and a post-transition stage. Those correlations compute the oxidation rate using the metal-oxide interface temperature, and they were developed from autoclave tests and in-reactor operation, but no considerations for the irregularity of the geometry. A coolant channel model is coupled with those correlations and the effect of the heat conduction deterioration through the oxide layer is accounted for in computing the interface temperature that controls the oxidation rate.

The corrosion rate equations for M5TM [44][45] have the same formulations as Zry-4, but with different parameters being used.

A cubic rate law for corrosion-layer thickness as a function of time is applied until a transition thickness of 7 micron:

$$\frac{ds}{dt} = \left(\frac{A}{s^2}\right) \exp\left(\frac{-Q_1}{RT_1}\right) \quad (\text{Eq. 13})$$

Where,

| | | | |
|----------------|---|-----------------------------------|------------------------|
| ds/dt | = | oxidation rate | (μm/day) |
| A | = | 6.3x10 ⁹ | (μm ³ /day) |
| s | = | oxide thickness | (μm) |
| Q ₁ | = | 27,446 | (cal/mol) |
| R | = | 1.987 | (cal/mol-K) |
| T ₁ | = | metal-oxide interface temperature | (K) |

After the transition thickness is reached, a flux-dependent linear rate law is applied with the rate constant being an Arrhenius function of oxide-metal interface temperature:

$$\frac{ds}{dt} = (C_0 + U(M\phi)^P) \exp\left(\frac{-Q_2}{RT_1}\right) \quad (\text{Eq. 14})$$

Where,

| | | | |
|---------|---|---|--------------------------------|
| ds/dt | = | oxidation rate | ($\mu\text{m/day}$) |
| C_0 | = | 8.04×10^7 | ($\mu\text{m/day}$) |
| U | = | 2.38×10^8 | ($\mu\text{m/day}$) |
| M | = | 1.91×10^{-15} | ($\text{cm}^2\text{-sec/n}$) |
| ϕ | = | fast neutron flux ($E > 1 \text{ MeV}$) | ($\text{n/cm}^2\text{-sec}$) |
| P | = | 0.24 | (-) |
| Q_2 | = | 29,816 | (cal/mol) |
| R | = | 1.98 | (cal/mol-K) |
| T_1 | = | metal-oxide interface temperature | (K) |

The high temperature oxidation rate for Zr-Nb is expected to be same, and the existing correlation in the code will be used for the accident condition modeling [17-18].

This implementation has been verified using regression test cases for both pre- and post-transition oxidation. Figure 22 shows the comparison of the oxide layer thickness computed using different corrosion models.

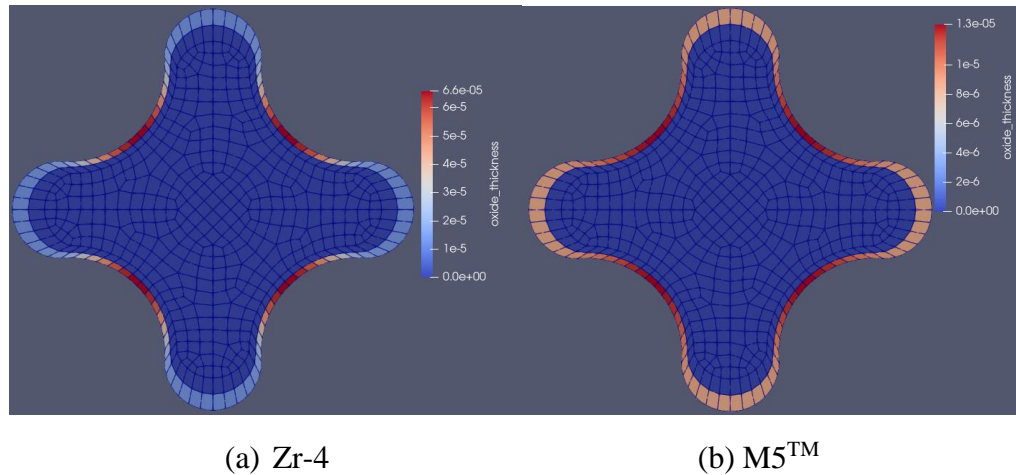


Figure 22: Non-uniform oxidation predicted by BISON code using a) Zr-4 model and b) A newly implemented Zr-Nb oxidation model

Although those models are adequate for modeling the cylindrical fuel pin, using this method to model Lightbridge's fuel design assumes the oxidation progresses in the direction normal to the cladding surface, and it would neglect oxygen diffusion in the azimuthal direction. Given the non-uniform distribution of heat flux and temperature, the oxidation rate would also be non-uniform. This non-uniform oxidation in the azimuthal direction is observed from the simulation as shown in the examples below. We still use this modeling approach for, a) although this is a generalization of the method for cylindrical pin, it provides a conservative estimate of local oxide layer thickness, b) no experimental data to develop a model that accounts for the geometric effects, and c) the hydrogen picked up from

water-side corrosion would diffuse under temperature gradient, and hydride precipitate could be less localized than oxide.

Hydrogen uptake in Zirconium alloys has been the object of extensive studies in different forms, varying from simple correlations using fuel rods PIE data to laboratory autoclave experiments using sheet and tube samples. While hydrogen uptake is strongly influenced by the alloy's general composition, Niobium is found to be the most important variable in determining both aspects of the corrosion process, namely, the weight gain or oxide thickness and the hydrogen uptake fraction. Unfortunately, none of the available data from both sources, irradiated fuel rods and laboratory experiments, can be directly applied to Lightbridge Zr-1Nb cladding without some degree of adaptation. Conventional LWR fuel types, namely, Zr-2, Zr-4, ZIRLO, and M5, all except Zr-4 contain varying amounts of Niobium plus some other elements such as Cu, Fe, Sn and Cr. Lightbridge metallic fuel elements cladding are made from a Zr-1Nb alloy, which in this regard is equal to M5 and E110, but may differ in the other alloying elements, which are unknown.

Given the degree of variability and scatter among the fuel rod data, we found it more appropriate to develop the equations for the hydrogen uptake model based on laboratory autoclave data and validate the model using fuel rod data, guided in the process by experience and judgment in interpreting the laboratory autoclave data.

The source of the experimental data used in the present development is the work by Arthur Motta, his students and other colleagues [46-47]. Oxidation kinetics follow a power law [48] of the form: $\delta = K t^n$, where δ is the oxide thickness, K is a rate constant, and n is the pre-transition (pre-breakaway) exponent that depends on the material. By fitting the weight gain data to a power law, the exponent n has been determined for the various zirconium alloys [48]. An example of this fit and the values of n from Reference [48] are displayed in Figure 23. As shown in Figure 23, Zr-1Nb alloy is not included, but an n -value of 0.28 can be derived for this alloy as the average of pure Zr and Zr-2.5Nb. Using $n=0.28$, the 100-day weight gain is 14.8 mg/dm^2 , as plotted in the figure, compared to 40 mg/dm^2 for ZIRLO sheet alloy. Using the conversion factor of $1 \mu\text{m}$ per 14.77 mg/dm^2 recommended in Reference [47], the equivalent oxide thickness is $1 \mu\text{m}$. To make use of this information for Zr-1Nb Lightbridge cladding, one can only conclude that the hydrogen uptake fraction for the Lightbridge cladding would be very low. Unfortunately, an oxide thickness of $1 \mu\text{m}$ is too small to extrapolate to higher weight gain (longer oxidation time), as shown in Figure 24 from Reference [46].

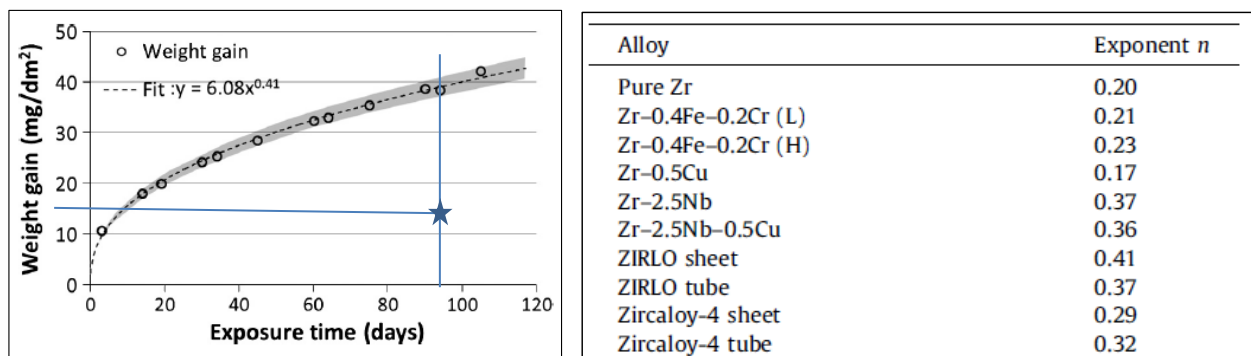


Figure 23: Power law representation of oxidation kinetics. Left: Power law fit of the pre-transition regime of ZIRLO sheet alloy [47]; Right: Exponent n from pre-transition (or pre-breakaway) power law fits of the different alloys [48].

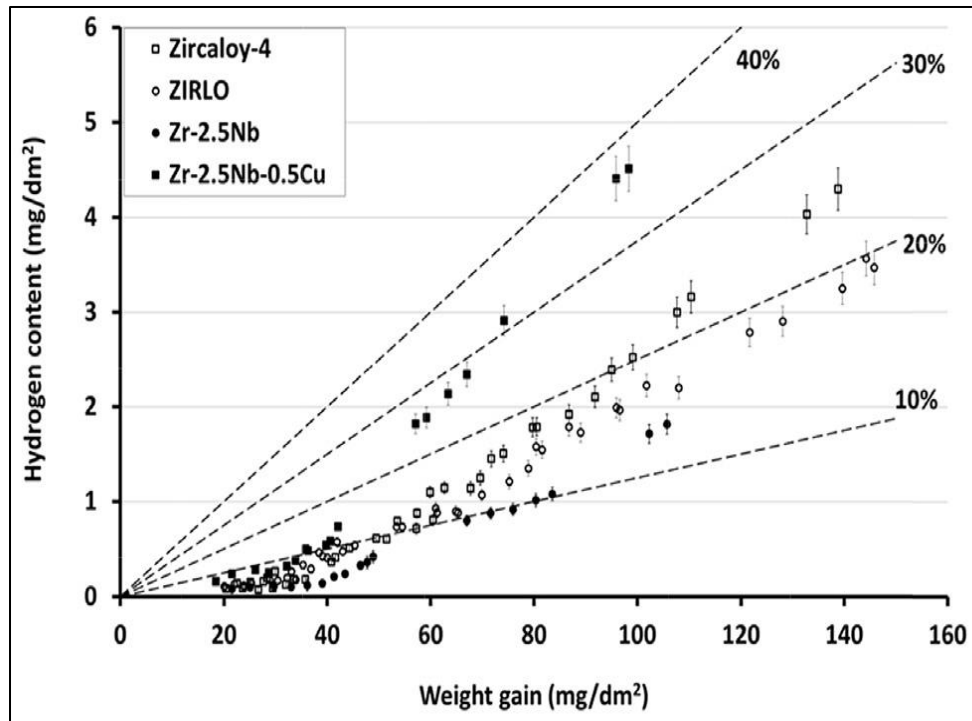


Figure 24: Hydrogen content versus corrosion weight gain (proportional to oxide thickness) during autoclave testing of various alloys in pure water at 360°C [46-47]

The oxidation-kinetics approach to hydrogen uptake discussed above, while highly instructive, cannot be extrapolated to post transition regimes where higher weight gains prevail. Therefore, we are forced to follow a semi-empirical approach by adapting Figure 24 to the Zr-1Nb alloy. As noted from Figure 24, the Zr-2.5Nb data follows a non-linear relation, showing very low hydrogen uptake for weight gain below 40 mg/dm², then begins to rise and follow a linear trend to about 110 mg/dm². On the other hand, the ZIRLO data follows similar, but higher, hydrogen uptake trend in the low range of weight gain, increasing linearly to about 150 mg/dm². The Niobium content of ZIRLO is not precisely known but reported (in the patent application) to be in the range of 0.5 - 2%. On this basis, we assume that Zr-1Nb would fall halfway between ZIRLO and Zr-2.5Nb. Using this assumption, we re-constructed a bilinear curve for Zr-1Nb as shown by the pink lines and the equations in Figure 25.

Now it remains to recast Figure 25 in a form that can be easily applied. This is done by replacing the horizontal and vertical variables by their equivalence, namely, oxide thickness for the weight gain and hydrogen content in ppm instead of mg/dm². The resultant equation is:

$$H = \begin{cases} 0.735t_{ox} & , \quad t_{ox} \leq 2.5 \\ 3.9235t_{ox} - 8.686, & t_{ox} > 2.5 \end{cases} \quad (\text{Eq. 15})$$

Where, t_{ox} is the oxide thickness (μm), H is hydrogen content (ppm).

For the example of Zr-4, the average hydrogen content at end of life is about 600 ppm data for 80 μm oxide thickness. We would expect that the hydrogen content for alloy Zr-1Nb, which is similar to M5TM, to be far less based on data comparison between Zr-4 and M5. Using Eq.15, we obtain for the quantity 305 ppm as the average hydrogen content, which qualitatively validates the model.

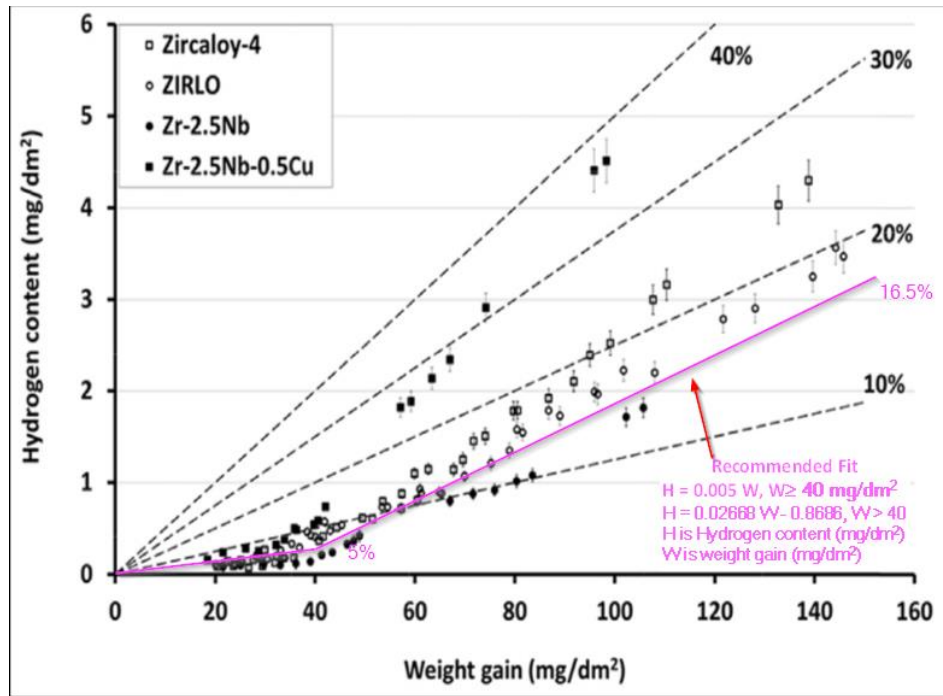


Figure 25: Hydrogen uptake versus weight gain for Zr-1Nb (Pink lines)

2.3 Coolant Channel Model

BISON code has a simple coolant channel model which can be used to establish thermal boundary conditions. This coolant channel model had been examined and tested for its validity on the modeling of this special fuel configuration.

Non-uniform cladding heat flux is found in the output from BISON code. This was compared to a finite element fuel code PEGASUS™, and both codes compute similar peak to average ratio of heat flux as shown in Figure 26. It is worth noting that this code-to-code comparison verified a behavior that is caused by the multi-lobe geometry, but not related to the coolant channel model in BISON.

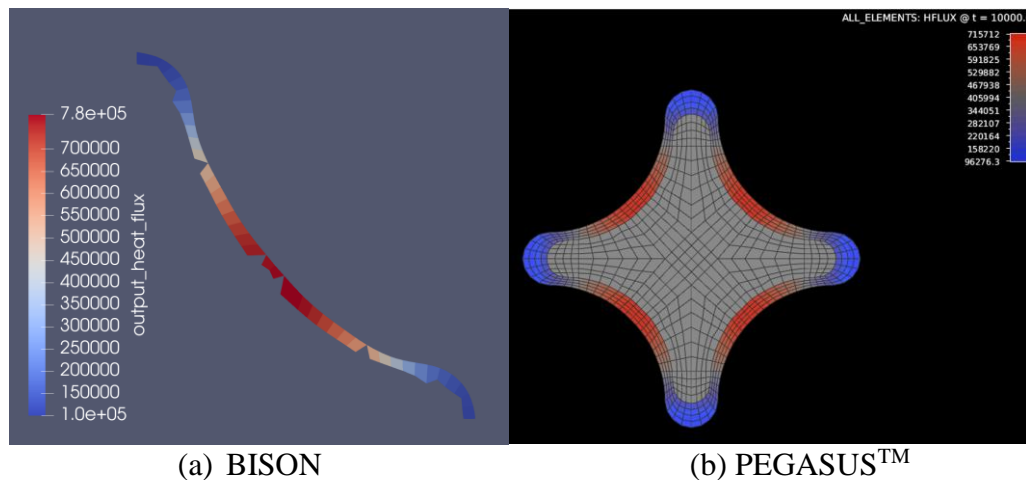


Figure 26: Comparison of cladding heat flux from BISON and PEGASUS code

For a non-uniform heat flux distribution, the critical heat flux is reduced using a factor f [49].

$$f = \begin{cases} 0.1 & \text{for } 1.0 \leq q''_{\max}/q''_{\text{avg}} \leq 1.5 \\ 0.2 & \text{for } 1.5 \leq q''_{\max}/q''_{\text{avg}} \leq 2.0 \end{cases} \quad (\text{Eq. 16})$$

where, q''_{\max} is the peak heat flux and q''_{avg} is the average azimuthal heat flux.

From the results of the heat flux distribution in a planar geometry in Figure 26, the reduction factor f in Eq. 16, is 0.2. Therefore, the critical heat flux would be reduced by 20% for this four-lobe metal fuel geometry.

From the several CHF correlations in BISON, BIASIS correlation which can be used for subcooled and saturated boiling conditions was chosen for the modeling analysis.

The helical geometry fuel could enhance the cross flow in the fuel assemblies. A simple correlation is given as:

$$\beta_{\text{eff}} = 0.29 \tan\theta + 0.0056 \quad (\text{Eq. 17})$$

Where, θ is the angle of the rod twist and β_{eff} is the mixing coefficient used in computing the rod bundle cross flow per unit length (kg/m-s) shown in Eq. 17, where S is the rod gap width (m), and G is the axial mass flux (kg/m²-s) [20].

$$w'_{ij} = \beta_{\text{eff}} SG \quad (\text{Eq. 18})$$

This needs to be considered for a more detailed thermal hydraulics modeling of the metal fuel, e.g., in a sub-channel code, but this cannot be simply adopted in the fuel performance code BISON. The helical geometry fuel could also have higher pressure drop across the coolant channel [20][21], but it is also suitable for a thermal hydraulics modeling using a sub-channel code, and is neglected in the current study. Therefore, only the reduction of critical heat flux can be accounted for in the analysis.

A few code modifications to the coolant channel model include a) adding a flow direction input to allow the use of mesh files created with different coordinate systems; b) an axial scaling and offset are added in the coolant channel model method to model with the fuel with reduced axial dimension; and c) modification to compute coolant enthalpy and temperature at a specified axial location.

3. BISON MODELING

The helical geometry metal fuel in current study is not axisymmetric, therefore, the conventional 2-D grid for the cylindrical fuel is not applicable. Although, it is a straightforward thinking to use 3-D grid for the finite element modeling; in practice the mesh density and computational time must be given careful consideration in the application. We took advantage of BISON's multi-dimensional capabilities and developed both 2-D and 3-D finite element grids for the modeling work.

3.1 Finite Element Models

- Two-dimensional planar geometry

This metal fuel design is a four-lobe geometry twisted around and extruded along the axis normal to the four-lobe plane. Therefore the 2-D four-lobe cross-section at any axial location has the same geometry. This cross-section is modeled using 2-D finite element grid for studying the thermal and mechanical responses of the metal fuel.

Figure 27 below shows the 2-D finite element grids created for the metallic fuel. With this 2-D grid, plane strain or generalized plane strain model can be used for the 2-D modeling analysis. While plane strain model assumes a zero out-of-plane strain, it creates high out-of-plane stress, and affects the effective (von-Mises) stress in the analysis. In comparison, the generalized plane model requires the uniform axial strain (out-of-plane) in fuel and cladding respectively, and resultant stresses and strains might be closer to the actual state of the deformed material. In the current study, we used generalized plane strain model exclusively for the 2-D modeling.

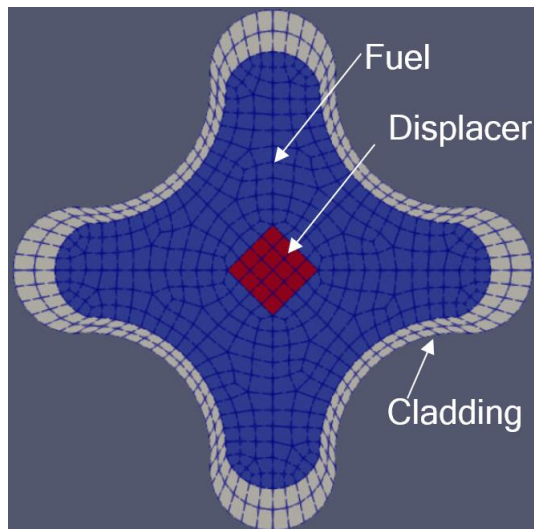


Figure 27: 2-D finite element grid for four-lobe metal fuel

- Multi-slice Model for Rod Analysis

A natural extension of the 2-D planar geometry is to duplicate the 2-D plane along the rod length direction, and to apply appropriate thermal and mechanical boundary conditions in each plane geometry at different axial locations to account for the axial variation in the linear heat generation rate, the coolant temperature, the thermal hydraulic conditions and the presence/absence of rod-to-rod contact. Therefore, this approach creates a multi-slice simulation of the fuel rod as shown in Figure 28.

This multi-slice model enables us to model the response of the whole fuel rod in a single analysis. Of course, this approach is still subject to the limitation of the 2-D assumptions in each plane, i.e., the analysis on each plane is not coupled with the thermal and mechanical responses on other planes.

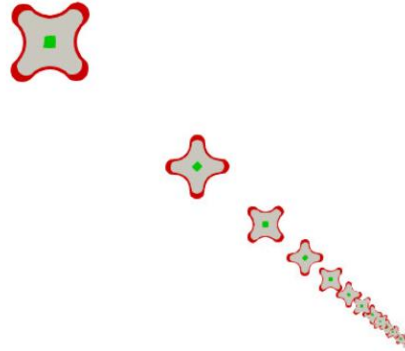
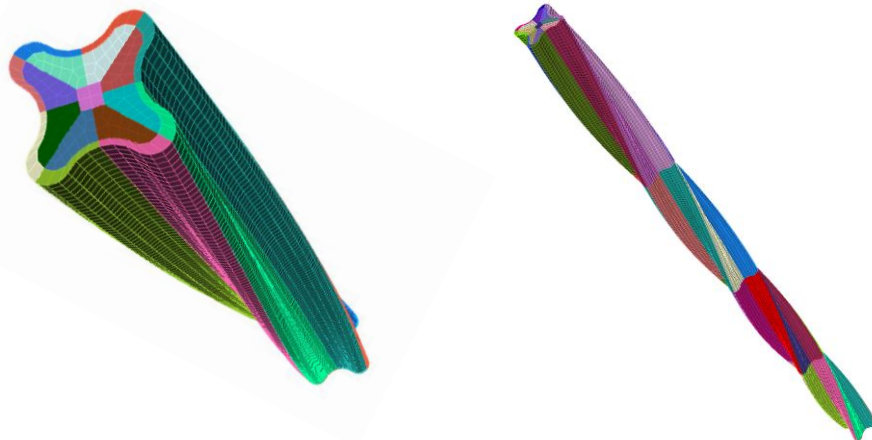


Figure 28: 2-D multi-slice grid for helical four-lobe metal fuel

- 3-D Fuel Rod Segment



(a) One twist

(b) Four twists

Figure 29: 3-D rod segment grids for helical four-lobe metal fuel

Since 3-D modeling can be computationally intensive, it may not be practical to use 3-D modeling for the full-length rod. Instead, we created the 3-D partial-length single-twist segment finite element grid as shown in Figure 29 (a). This segment can be duplicated to model a full-length fuel rod with multiple twists.

This model segment can be used in multiple runs to calculate the metal fuel responses at different axial locations of the fuel rod. Uniform strains are assumed at the top/bottom planes of the rod segment and corresponding boundary condition is applied in BISON input.

- Rod-to-Rod Contact Modeling

Along the length of the fuel rod, at certain axial locations, the rod-to-rod contact would constrain the lateral movement of neighbor rods. A shroud outside of the fuel assembly would hold all fuel rods and provide the constraint of the lateral displacement of all fuel rods at the rod-to-rod contact planes. To account for this, the boundary conditions at those planes in 3-D or 2-D multi-slice models are added to constrain the movement of the fuel rod at those planes.

- Fuel-cladding Interface

A co-extrusion process metallurgically bonds the fuel and cladding materials. In the current modeling work, the fuel core and the cladding are assumed to be perfectly locked at the interface; there is no slip between fuel and cladding in the axial or tangential directions.

A few scripts for generating the 2-D, 2-D multi-slice and 3-D segment finite element grids using CUBIT software are shown in Appendix. C.

3.2 BISON Code Modification

In addition to the new material model implementations (mainly for U-Zr fuel), a number of code modifications were also made in BISON to support the analysis using the abovementioned finite element models.

The 2-D single plane and the 3-D segment model need only the input power and computed coolant conditions at specified locations. Note that there is no fission gas release, each slice in the 2-D plane model or a 3-D segment is modelled independent of geometries outside of those entities.

Therefore, the axial scaling and axial offset are enabled in the power and coolant channel models in BISON. With those updates, the 2-D plane model or 3-D segment model can be applied to any specified axial location.

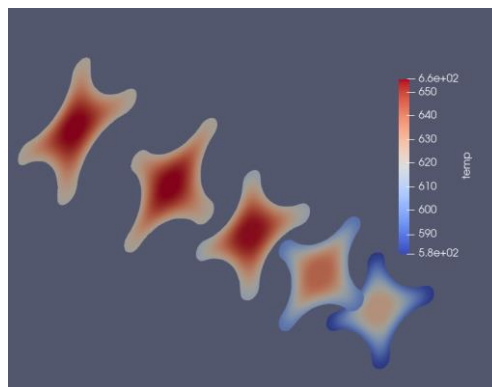


Figure 30: Temperature contour of a multi-slice geometry using modified coolant channel model

Figure 30 shows the temperature contour of a multi-slice model with above code modifications.

4. MODELING RESULTS FOR NORMAL OPERATION

4.1 Base Case Description

Since there is no operating history for metal fuel in an LWR environment, we created a case under an idealized condition. Assuming a metallic fuel with design geometry shown in Figure 1 and Figure 2 in Section 1 can be used to replace the UO_2 fuel rod with same linear power history and irradiation, a base case is created by modification of the irradiation history and operating conditions for a PWR UO_2 fuel rod. The linear power and axial power profiles are shown in Figure 31 and Figure 32 respectively. The coolant conditions are described in Table 7.

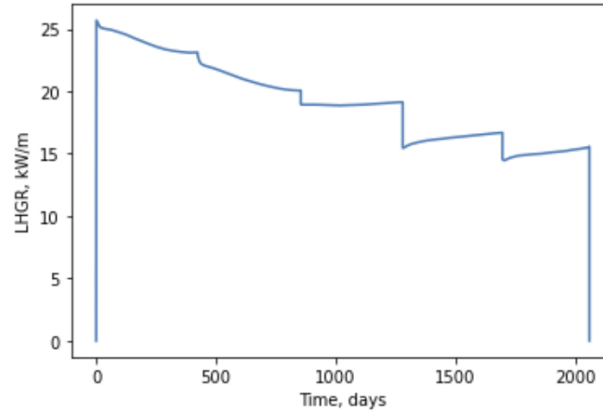


Figure 31: Rod average LHGR for the modeling case

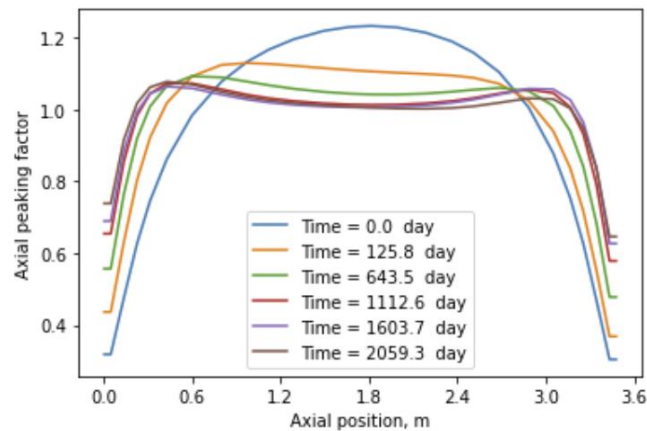


Figure 32: Axial peaking factors at different times

Table 7: Coolant channel input parameters

| Parameters | Value |
|--|-------|
| System pressure (MPa) | 15.5 |
| Inlet temperature (°C) | 285 |
| Rod to rod pitch (cm) | 1.26 |
| Coolant mass flux (kg/m ² ·s) | 3600 |

UO₂ fuel under such an irradiation history would have an equivalent rod average burnup of 81 GWd/tU, which is 30% higher than the current licensing limit.

A multi-slice model is used to model the global response of the metal fuel design. A total of 20 X-Y planes are equally distributed along the longitudinal direction of the fuel rod. Those plane geometries are modeled using the generalized plane strain formulation in BISON to represent local fuel slices sampled at different axial locations. The global fuel response including fuel temperature, fuel dimensional changes, stresses, and cladding corrosion are examined.

A segment of the fuel rod at the mid-height location is also modeled using 3-D geometry to examine the detailed mechanical responses. Boundary conditions are applied to restrict rigid body motion in 3-D geometry. The top of the segment is modeled by enforcing a uniform axial displacement at the top surface.

The equivalent UO₂ fuel case with cylindrical geometry is also examined for comparison to important performance parameters.

4.2 Results

4.2.1 Burnup

The average burnup at the mid-height location is 17% FIMA. Although it is anticipated that the absorption of epithermal neutrons could result in a higher concentration of fissile materials contributing to radial power and burnup peaking in the peripheral region of the fuel core, we do not have sufficient information to develop a model to account for this. A constant profile on the X-Y plane is assumed in the analysis, and this would predict a higher peak fuel temperature compared to a case with radial power peaking.

4.2.2 Fuel Temperature

The temperatures at centerline, cladding valley and lobe tip locations at the mid-height position is shown in Figure 33 below for the base design. An axial temperature profile in comparison to UO₂ fuel with a cylindrical geometry at the beginning of life (BOL) is shown in Figure 34. Comparing to the UO₂ fuel design, the metal fuel case exhibits a much lower temperature due to the absence of a fuel-cladding gap and the high thermal conductivity of metal fuel. It also exhibits a much-flattened axial temperature profile as compared to the UO₂ case.

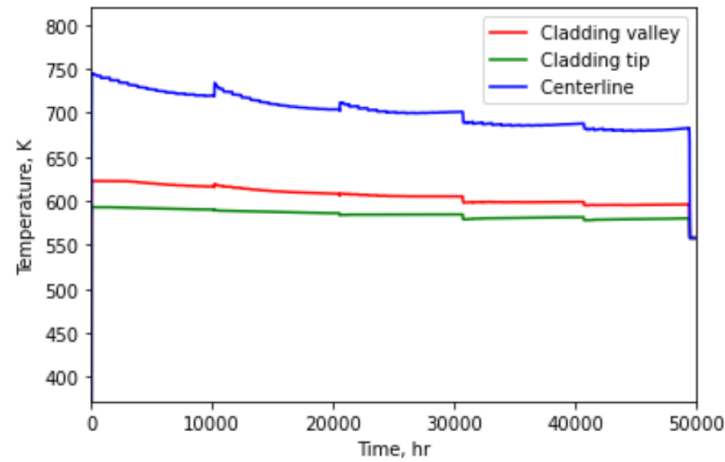


Figure 33: Temperatures at centerline, cladding valley and tip at mid-height location

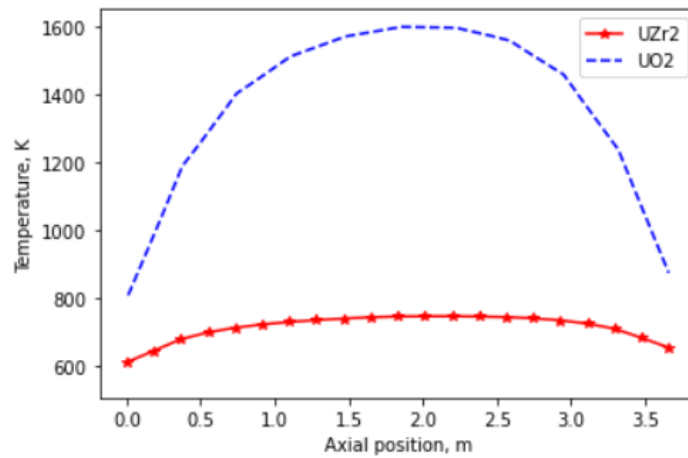


Figure 34: Axial profile of centerline temperature in comparison to UO₂ fuel at BOL

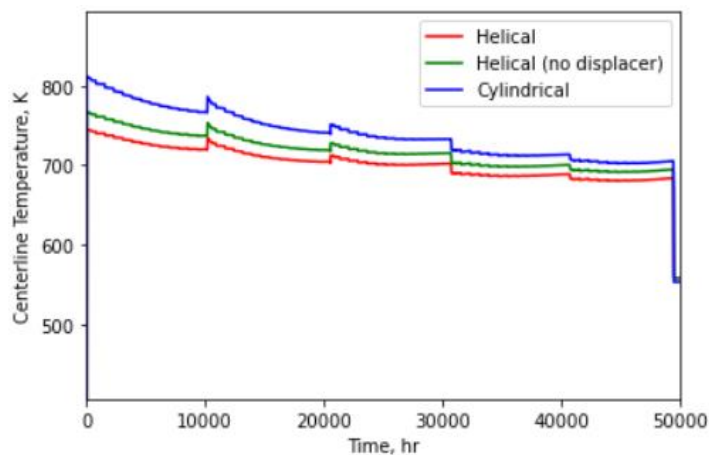


Figure 35: Comparison of centerline temperatures with different fuel configurations

To examine the effects of the central displacer and the fuel design geometry on the fuel temperature prediction, a case without the displacer and an equivalent cylindrical geometry case were also run with the same linear power input. Results are shown in Figure 35. Using a cylindrical shape without a displacer predicts a centerline temperature that is 66 K higher than the base case at BOL. Comparing

to a helical fuel design without displacer, the centerline temperature difference is ~30 K higher than the base case.

4.2.3 Cladding Corrosion

In modeling cladding oxidation under operating conditions, we used a material model for M5TM, which might be closer to the composition of the Zr-1%Nb cladding alloy used for this fuel design. The current material model in BISON is only applicable for Zr-4 type cladding used in PWR which predicts significant cladding oxidation, and this would not have any credits for the high corrosion resistance alloy used in the reactor. For the base case, we ran both corrosion models and the peak oxide thickness at the mid-height position is 14 microns using the M5TM model as compared to 104 microns predicted using the corrosion model for Zr-4 in BISON.

Figure 36 shows that this fuel design, having higher heat flux at the valley location, has non-uniform oxidation predicted by the model, with the maximum oxide layer thickness predicted to be 50% greater than the minimum oxide layer thickness at the tip of the lobes.

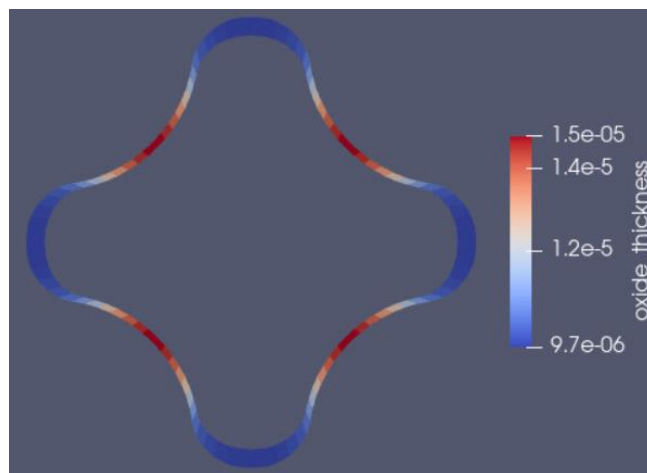


Figure 36: Non-uniform cladding oxidation at mid-height location

Figure 37 provides the maximum clad oxidation for the base case in comparison to an equivalent cylindrical UO₂ fuel design. The maximum oxide layer thickness is ~15% greater than the case with cylindrical fuel. With 20-micron thickness of oxide, the hydrogen uptake is estimated to be ~100 ppm. The cladding corrosion and hydrogen uptake from current modeling results seem low, but this is mainly due to the use of a model for a high corrosion resistance alloy.

The cladding temperature distribution is also not uniform; however, the valley temperature is slightly higher, and hydrogen absorbed could diffuse from the valley to the tip along the temperature gradient. Therefore, it may compensate partly to the non-uniform of the oxidation. Hydrogen diffusion and precipitation would also depend on the stress gradient in the cladding, and those were not modeled in current study.

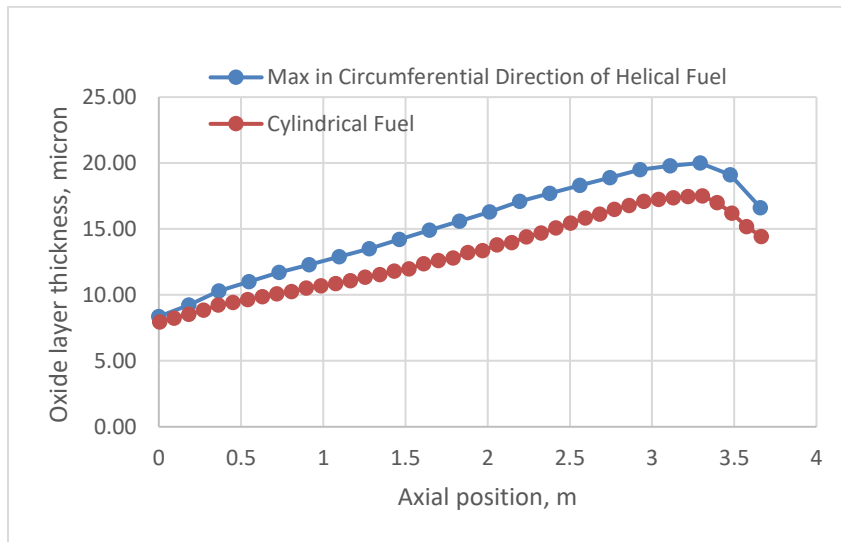


Figure 37: Axial cladding oxidation profile in comparison to UO_2 fuel

4.2.4 Dimensional Changes

The following dimensional changes are examined for the base case:

- The volume changes in fuel, cladding, and displacer,
- The strain distribution,
- The maximum local dimensional changes, and
- The axial dimensions.

Figure 38 shows the deformed fuel geometry at end of life (EOL) compared to the original geometry on the X-Y plane. The valley deforms more than other regions. At EOL, the radial displacement at the cladding tip is 290 microns while the radial displacement at the valley is 890 microns, roughly three times the displacement at the cladding tip.

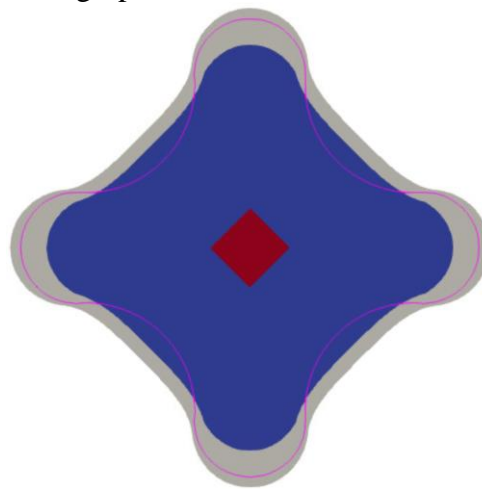


Figure 38: Fuel deformation in comparison to original contour (in pink curve)

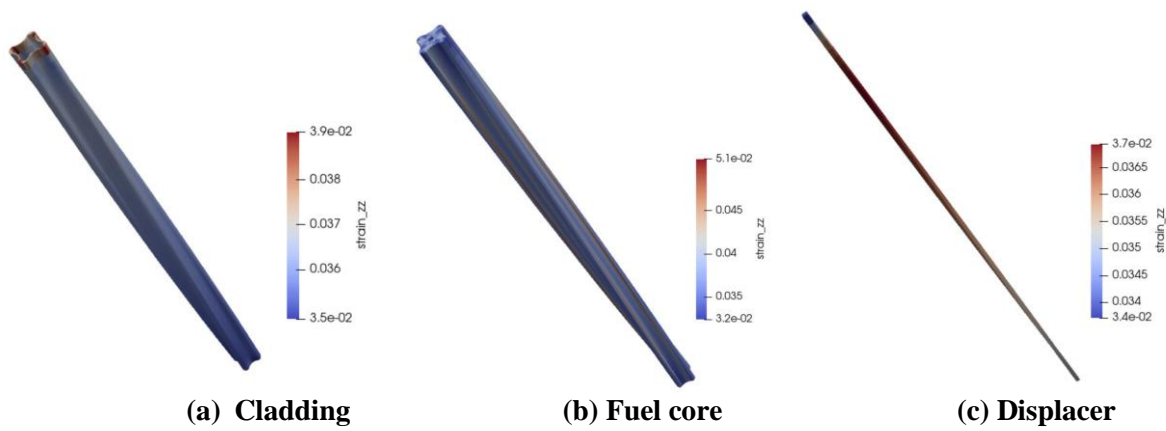


Figure 39: Axial strain contour in different fuel components at EOL

Figure 39 shows the axial strain contour at EOL. The axial strain in the cladding near the top surface appears slightly higher, which might be caused by numerical error near the end of the segment. The fuel axial strain ranges from 3.2% to 5.1%, and the high strain appears to be near the edge of the lobe. The axial strain in the displacer has also shown some variations.

Table 8 summarizes the fuel dimensional changes with different modeling options. The fuel dimensional change is evaluated as the ratio of the fuel volume or area (2-D cases) at shutdown condition to the initial values. Table 8 also lists the results accounting for constraints on fuel swelling due to the interaction with neighboring rods.

Table 8: Fuel dimensional changes at EOL

| | Fuel core solid/solid + gaseous | Total Volume solid/solid + gaseous |
|--------------------------------|------------------------------------|---------------------------------------|
| Plane (no-constraint) | 1.243 / 1.347 1.158* / 1.27* | 1.161 / 1.227 1.104* / 1.17* |
| Plane (constraint) | 1.216 / 1.304 | 1.136 / 1.188 |
| 3-D segment (no-constraint) | 1.252 / 1.372 | 1.170 / 1.250 |

* Using 1% volumetric strain per 1% FIMA for solid swelling

Results in Table 8 shows that the cladding deformation partially accommodates the swelling of fuel core, and the total volume change is reduced by ~35% due to the constraint by cladding. The 2-D cases were run with/without constraint (rod-to-rod contact), and the rod-to-rod contact can also reduce a fraction of the fuel swelling. The 2-D case shows lower swelling since the metrics for the 2-D dimensional changes do not account for the axial strain, which is roughly 3% at EOL, and with that correction, it matches the 3D case result.

The dominant contribution is solid swelling, but the gaseous swelling contribution predicted by the model is appreciable, and it accounts for almost 30% of the total fuel swelling. Accounting for all those contributions, the total fuel dimensional change (volumetric) is 25%, and this is quite significant. Note that both solid and gaseous swelling models have uncertainty, more so for the latter. We also ran a case assuming 1% solid swelling per 1% FIMA and neglected the gaseous swelling, the total dimensional change is reduced to 18% from 23% for the 2-D case.

In addition, a comparison of the helical fuel design (2-D) with the cylindrical shaped fuel was also made as shown in Figure 40. Although the cylindrical fuel case has predicted higher fuel temperatures than the helical fuel, it has relatively lower fuel swelling than the four-lobe geometry.

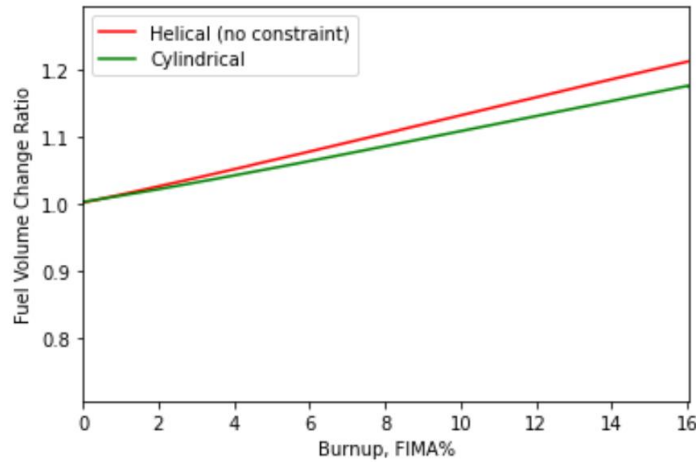


Figure 40: Comparison of fuel swelling with different geometries in 2-D cases

4.2.5 Cladding Stresses/Strains

The 3-D cladding stress contour at EOL is shown in Figure 41. The peak stress occurs at the tip location. Figure 42 and Figure 43 show the comparison of stress evolution for constraint (rod-to-rod contact) and non-constraint cases at the valley and the tip locations respectively; notice the reversal between the valley (Figure 42) and the tip (Figure 43). The initial high stresses in the constraint case are mainly caused by the contact forces due to the fuel thermal expansion but are reduced rapidly presumably by the creep of fuel and cladding. After that, the fuel swelling can continuously push the cladding while the cladding creep could partially relieve the stress. The magnitude of the stress is not sufficient to reach the yield strength of the zirconium alloy.

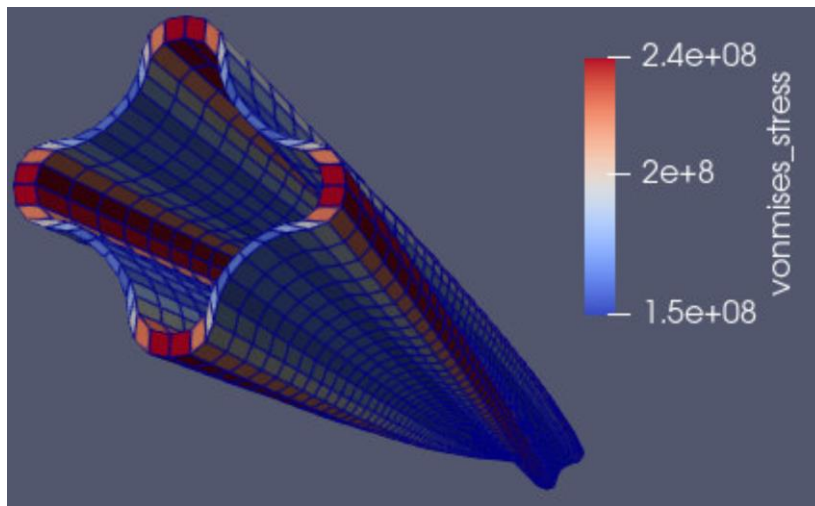


Figure 41: Cladding von-Mises stress contour at the EOL

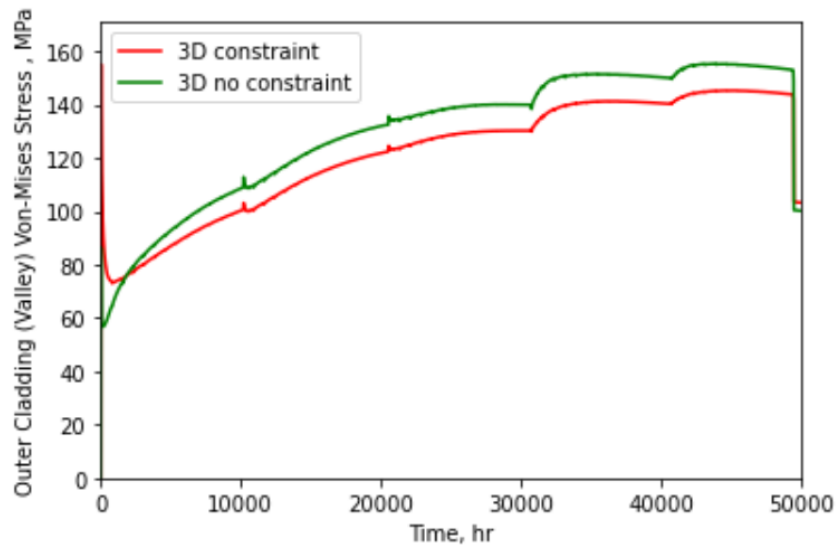


Figure 42: Cladding von-Mises stress at the valley location

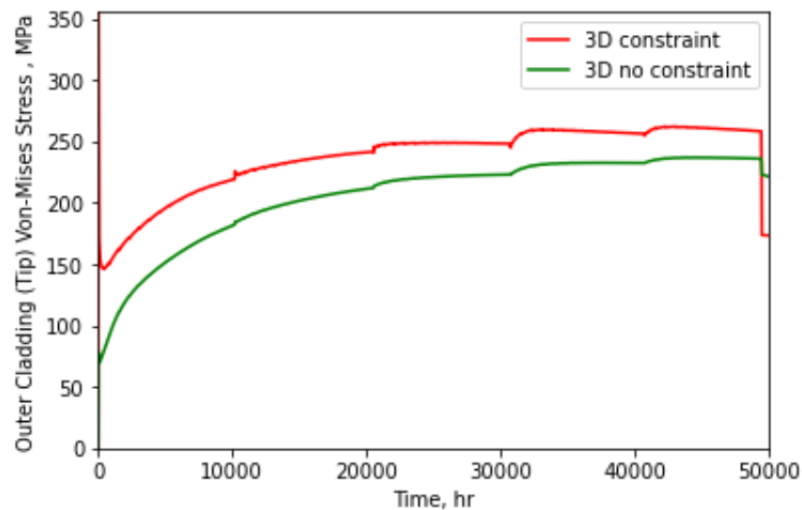


Figure 43: Cladding von-Mises stress at the lobe tip location

Figure 44 and Figure 45 show the cladding hoop strain and the axial strain for the 3-D (non-constraint) case. The valley location has accumulated more creep strain than the tip location. The axial strain is lower than the deformation strains on the X-Y plane, and is also, as expected, quite uniform.

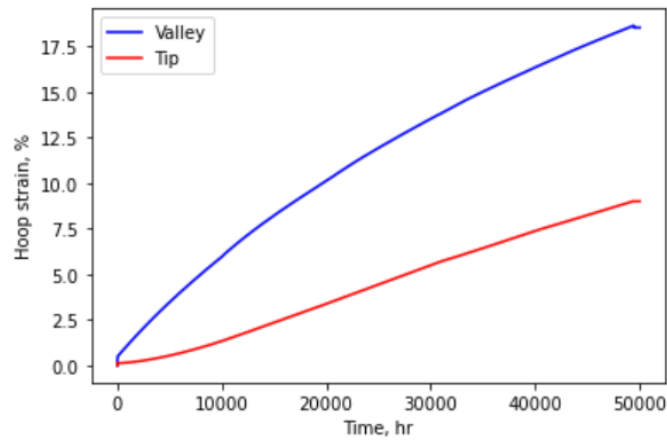


Figure 44: Cladding hoop strain at the valley and lobe tip locations

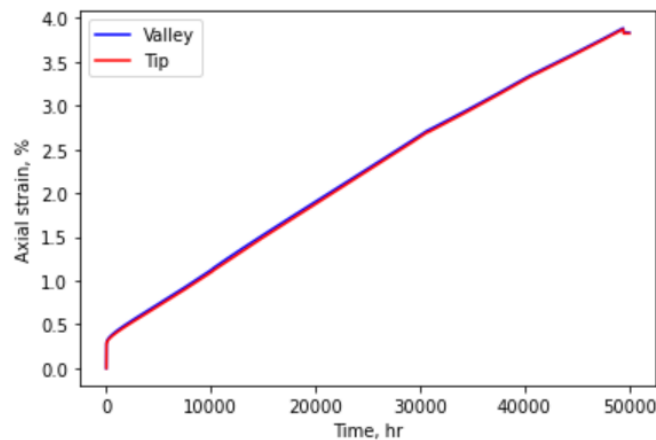


Figure 45: Cladding axial strain at the valley and lobe tip locations

4.3 Performance Metrics

In comparison to the ceramic UO_2 fuel in zircaloy tube, the fuel and cladding is metallurgically bonded and has no plenum and no gap. Therefore, there is no free volume to accommodate fission gas release. No fission gas release or rod internal pressure are considered as performance metrics.

The 1% strain limit (in SRP 4.2 [10]) for LWR UO_2 fuel is not applicable to the metallic fuel. A large dimensional change however does have implications on fuel performance. A few possible consequences are a) the axial growth of fuel rod that can potentially cause bowing as the rod growth could interfere with other components in the fuel assembly, b) differential axial growth of adjacent rods could violate the design function of inter-supporting of fuel rod at the self-spacing plane without using spacer grids, and c) the fuel swelling can cause the reduction of flow area, although this is relatively small and can be compensated by the fuel design which could allow larger flow area.

The fuel and cladding materials have similar linear thermal expansion such that temperature changes in the fuel is not significant and would not cause significant stress in the cladding. On the other hand, fuel swelling can continue to push the cladding outward. However, those stresses in the cladding can relax due to the creep and the stress changes are gradual. The highest stress is observed at the tip of cladding lobe location.

This large deformation in the cladding does not necessarily mean that the cladding can fracture and breach. The speculation is that the mechanical failure of cladding would still be governed by its ductility. Ref. [17] indicates there were some operating experiences for the metal fuel irradiated to high burnup in Russian marine reactors. This might offer some assurance of the operating feasibility even with fuel swelling, but we have found no information from public domain on the details about the operating condition or measurements to ascertain the failure limit.

It is important to note that in the absence of fission gas release and fuel-clad gap the stress corrosion cracking (SCC) failure mechanism is non-operable. This leaves hydrogen embrittlement and rod to rod fretting as potential failure mechanisms, with hydrogen embrittlement being of lower concern due to the relatively low hydrogen uptake.

Compared to cylindrical fuel, the corrosion in the metal fuel with four-lobed geometry exists, and the non-uniform heat flux could possibly cause a non-uniform oxidation as predicted by the model. Additional conservatism might be needed, but the actual performance would largely depend on the cladding ductility which needs to be determined from mechanical tests.

The bonding between the fuel and cladding is assumed to be perfectly “locked.” Heat transfer across the fuel/cladding interface is assumed to be continuous. Although no information was found on the bond strength for this fuel design, Ref. [8] shows that fuel-clad bond could weaken, and a gap could develop in hot-press bonded uranium-alloy fuel. This is not investigated in current study but could be a consideration for the fuel performance issue if this is detected from operation.

5. MODELING RESULTS IN ACCIDENT CONDITIONS

This section describes the modeling results of metal fuel in accident conditions. Recognizing that the study of accident behavior may often involve coupling the fuel performance code with a neutronic code or a thermal hydraulics code, and there are no results of thermal hydraulic and neutronic modeling readily available, we used BISON code to perform simplified studies with the aid of some existing input for UO_2 fuel cases in accident conditions. The accident scenarios for modeling metal fuel behavior includes the loss of coolant and reactivity insertion accidents.

5.1 LOCA Modeling

In a design basis loss of coolant accident (LOCA), depending on the rod decay power and the local heat transfer condition, the conventional UO_2 fuel rod with Zircaloy cladding used in LWRs could have fuel rod ballooning and burst, and cladding can be oxidized in high temperature steam and become embrittled. Current regulations specify temperature and oxidation limits to ensure coolable geometry during the accident and maintain the long-term capability to cool the core after the accident.

For the use of metallic fuel in LWRs, the absence of free volume (pellet-cladding gap and plenum) in the fuel system, fuel rod ballooning and burst are essentially ruled out. The concern remains on the fuel temperature escalation which may still cause oxidation of cladding and softening of metallic fuel.

This sub-section presents a simple analysis to compare the metallic fuel to the UO_2 fuel in a simulated LOCA condition. The reflood heat transfer correlations in BISON code are used to provide boundary condition for the modeling case. The analysis for the metal fuel is performed using 2-D plane geometry, and the UO_2 fuel is modelled using 2-D RZ geometry.

5.1.1 LOCA Case Description

We used an ANS decay heat model, and the decay power for the peak power node (45 kW/m) is shown in Figure 46. Figure 47 shows the coolant pressure change during the LOCA. The modeling case has the axial peaking of power at the mid-height location as shown in Figure 48. Results are examined at the peak power location for both metal fuel and UO_2 fuel.

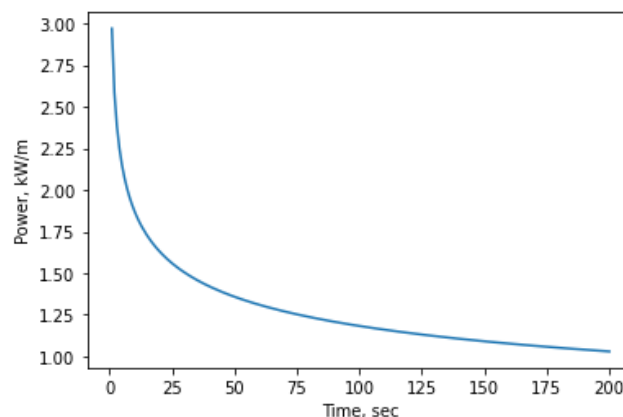


Figure 46: Decay power using ANS model (LHGR = 45 kW/m)

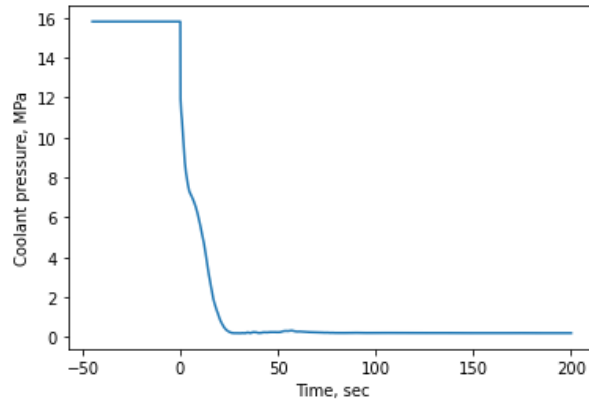


Figure 47: Coolant pressure in the simulated LOCA condition

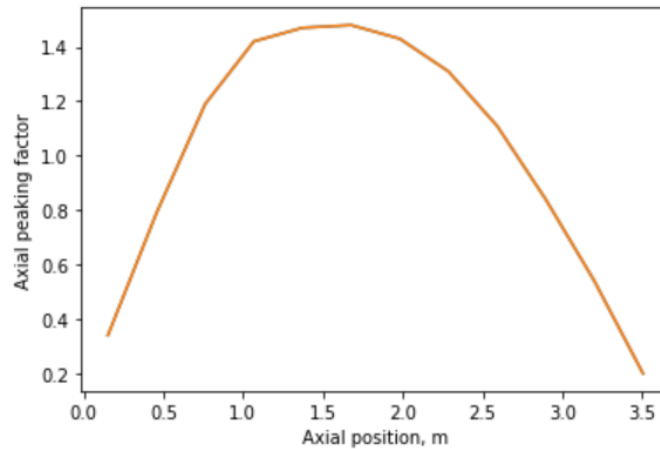


Figure 48: Axial power profile in the LOCA condition

Key parameters for the modeling the thermal hydraulics conditions during the LOCA is summarized in Table 1 below. The flooding time is varied to produced different peak cladding temperatures.

Table 9: Input variables on modeling the thermal hydraulics boundary conditions

| Parameter | Value |
|---------------------|---------------------------------------|
| Flooding time (s) | 5.0, 20.0, 60.0 |
| Flooding rate (m/s) | 0.05 |
| Axial location, (m) | 1.88 |
| Peak power, (kW/m) | 45.0 |
| Reflood mode | default, the correlation in Ref. [50] |

Figure 49 shows the heat transfer coefficient history at the cladding surface in a valley location.

Table 10: Input parameters for the UO₂ fuel case

| Parameter | Value |
|----------------------------------|-------|
| Pellet outer radius (mm) | 4.13 |
| Clad thickness (mm) | 0.61 |
| Fuel-clad gap thickness (micron) | 75 |
| Fill gas pressure (MPa) | 2.0 |

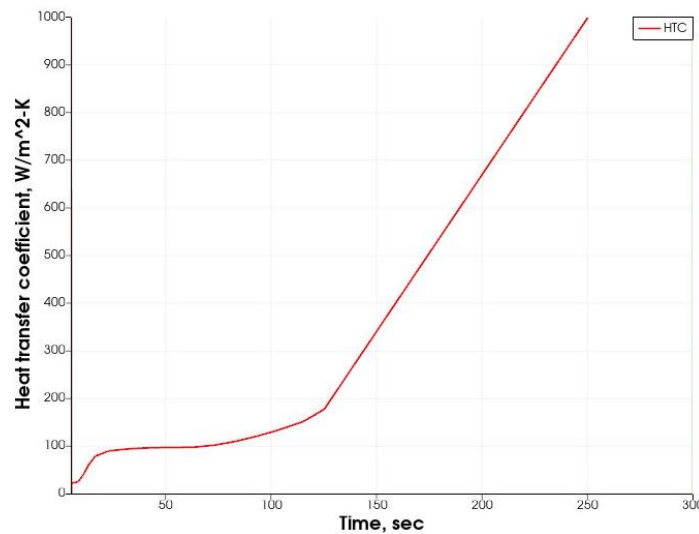


Figure 49: Clad surface heat transfer coefficient in a simulated LOCA condition at valley location (peak power = 45 kW/m, flooding time = 5 sec)

5.1.2 LOCA Modeling Results

Figure 50 - Figure 53 show cladding surface temperatures for UO₂ and metal fuel at various input conditions. Under all circumstances, metal fuel has lower peak cladding temperature and shorter duration at high temperatures. than UO₂ fuel. The comparison of the peak cladding temperature in all those cases are summarized in Table 11. It is interesting to note that the metal fuel seems to show a tendency for much shorter coping time than UO₂ fuel.

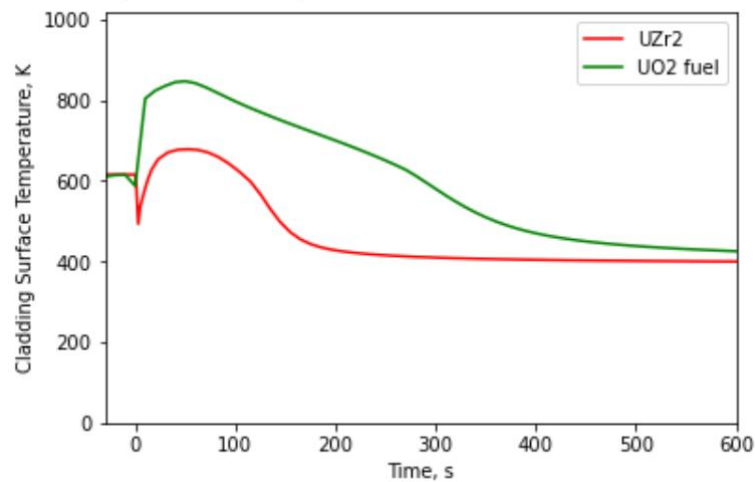


Figure 50: Cladding surface temperature during LOCA (power = 30 kW/m, flooding time = 5 sec)

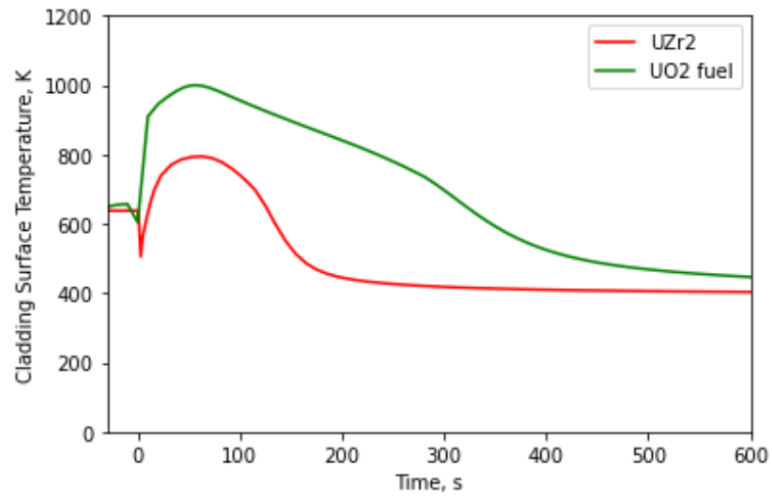


Figure 51: Cladding surface temperature during LOCA (power = 45 kW/m, flooding time = 5 sec)

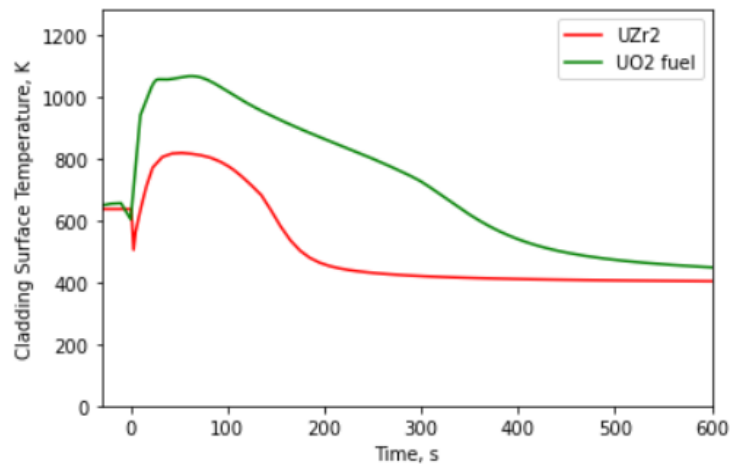


Figure 52: Cladding surface temperature during LOCA (power = 45 kW/m, flooding time = 20 sec)

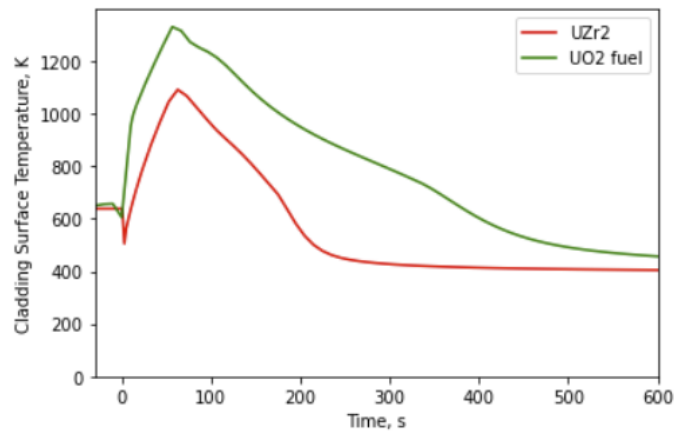
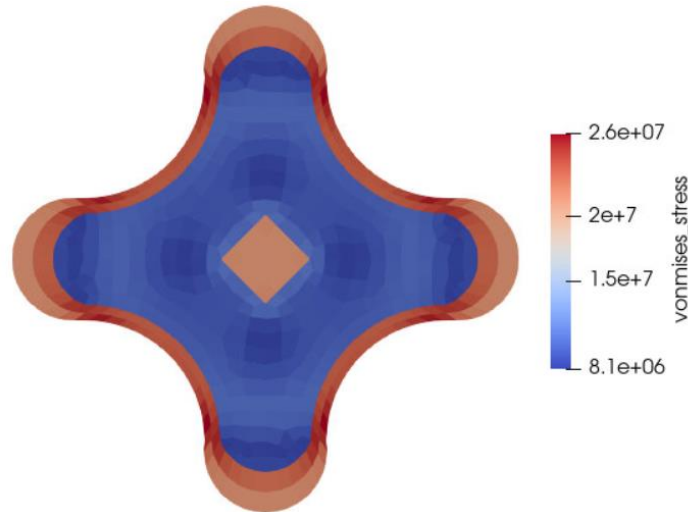


Figure 53: Cladding surface temperature during LOCA (power = 45 kW/m, flooding time = 60 sec)

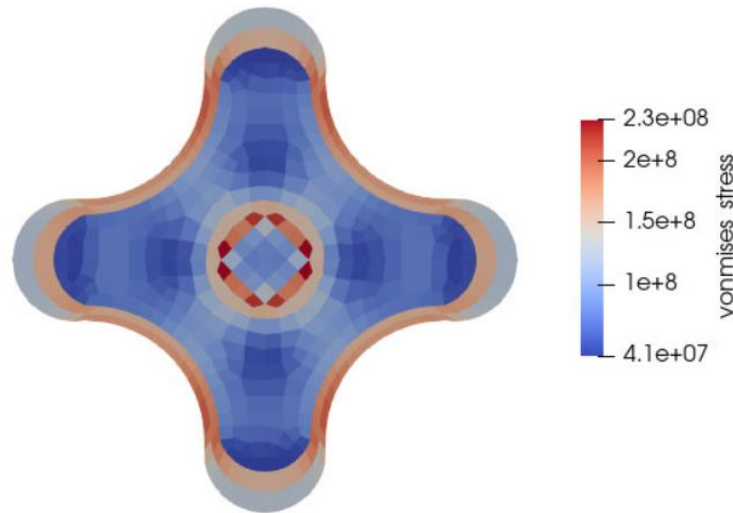
Table 11: Comparison of peak cladding temperature between UO₂ fuel and UZr₂ fuel

| | | | | | |
|-------------|--------------------|-----|------|------|------|
| Case | P_{\max} (kW/m)* | 30 | 45 | 45 | 45 |
| | t_f (sec)* | 5 | 5 | 20 | 60 |
| PCT* (K) | UO ₂ | 915 | 1000 | 1069 | 1330 |
| | UZr ₂ | 678 | 795 | 820 | 1094 |

* P_{\max} is peak power; t_f is flooding time PCT is peak cladding temperature

**Figure 54: Von-Mises stress contour at the time of PCT (power = 45 kW/m, flooding time = 60 sec)**

The von-Mises stress contour of metal fuel at the peak cladding temperature time is shown in Figure 54 for the case with a reflooding time starting at 60 sec. Figure 55 shows the stress contour right after cooling down. The cladding stress appears to be very low at the time of PCT, however, it is higher after the fuel and cladding cool down, but the cladding is in compressive state. Most likely, it is caused by the thermal contraction of the fuel which has larger thermal expansion coefficient than the cladding material.

**Figure 55: Von-Mises stress contour at the time of cooling down to 400 K (power = 45 kW/m, flooding time = 60 sec)**

The temperature was also examined; there is no discernable difference between fuel and cladding right after the start of LOCA. This is perhaps due to the low thermal inertia in this fuel: high thermal diffusivity in the fuel and absence of a fuel-cladding gap.

Due to both the lower cladding temperature and shorter duration at high temperatures, the cladding oxidation would also be lower than UO_2 fuel. The fuel fragmentation and dispersal in coolant could be an issue for high burnup UO_2 fuel in LOCA, but this is also eliminated in the metal fuel case.

There are possible conditions that the fuel temperature is significantly high, and it could reduce the mechanical strength, and the gaseous fission products can probably have enhanced diffusion and contribute to the fuel swelling. This however might be mitigated by a better cooling of the fuel. Those are not investigated in current work but could be of interest to future studies.

The work in Ref. [51] had a comparison between the UO_2 fuel and metal fuel using RELAP5 to compute cladding temperature for both VVER and PWR condition, and the difference in the PCT is even larger. The result on VVER is close to what is presented in Ref. [17]. The analysis using reflood correlation shows lower difference possible due to the simplifications in treating the fluid temperature in the heat sink, which is assumed to be same for both UO_2 and UZr_2 case. Therefore, coupling BISON with a thermal hydraulics code is warranted to have an accurate prediction of the fuel responses in such condition.

5.2 REA Modeling

5.2.1 REA HFP Case

A control rod ejection accident at hot full power (HFP) condition is modeled using BISON. The input power history and axial peaking factors are based on analysis data for light water reactor UO_2 fuel and zircaloy cladding materials from existing nuclear power plant.

The F_q value for this case is 2.7 and 3.7 prior to and after the transient. A constant multiplier of 3.7 is applied to the fuel rod throughout the REA. A fixed axial shape is assumed in current analysis. The input core power and axial power shape is shown in Figure 56 and Figure 57 respectively. We assume this transient power is applied to a fresh fuel condition. Therefore, the fuel swelling is neglected.

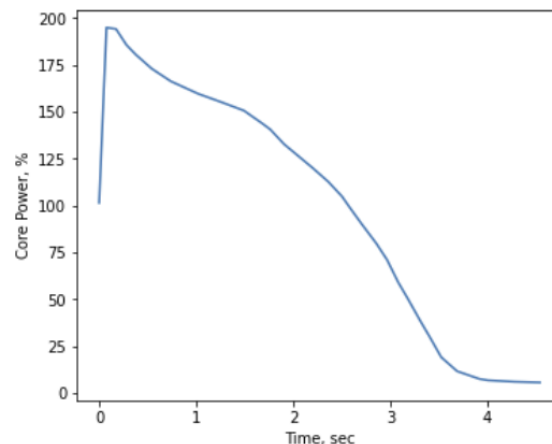


Figure 56: Core power in REA at HFP condition

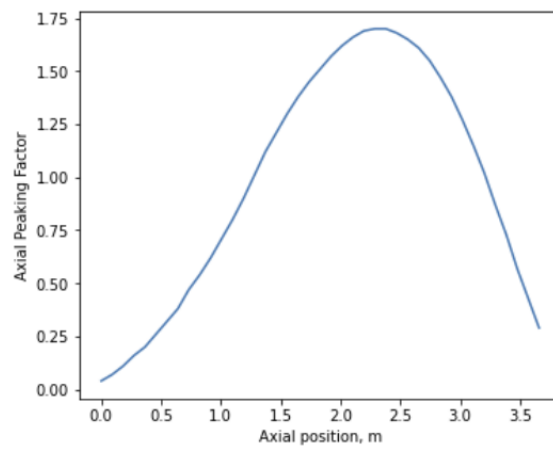


Figure 57: Axial power shape used in the REA HFP case

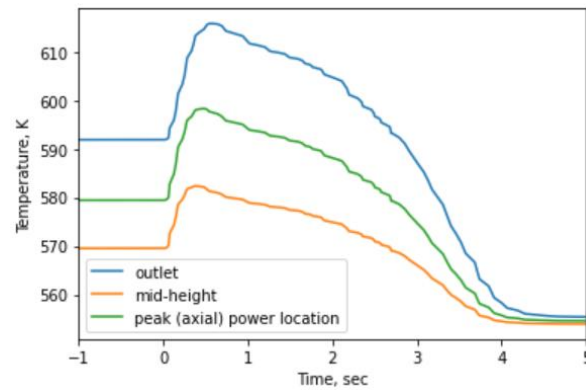


Figure 58: Coolant temperature calculated using BISON

Figure 58 plots the coolant temperature calculated using BISON code from the modeling of a full-length fuel rod problem. The coolant temperature history is used in the input thermal boundary condition a 3-D case modeling a segment of fuel rod at the peak power location (slightly above mid-height).

5.2.2 REA HFP Results

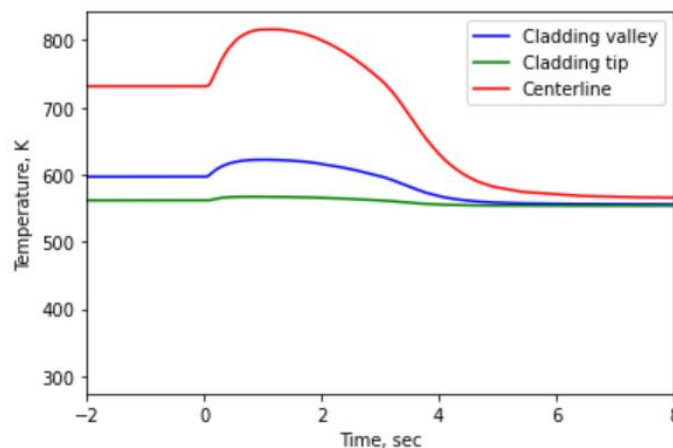


Figure 59: Fuel temperature change during an REA at HFP condition

Figure 59 shows the centerline temperature, cladding temperatures at the valley and tip locations during the REA. Figure 60 shows the temperature contour at the peak. Figure 61 shows the cladding output heat flux in comparison to the critical heat flux. The maximum heat flux at the valley location is

2.3 MW/m² and 0.49 MW/m² at the cladding lobe tip. The calculated critical heat flux is 5.25 MW/m².

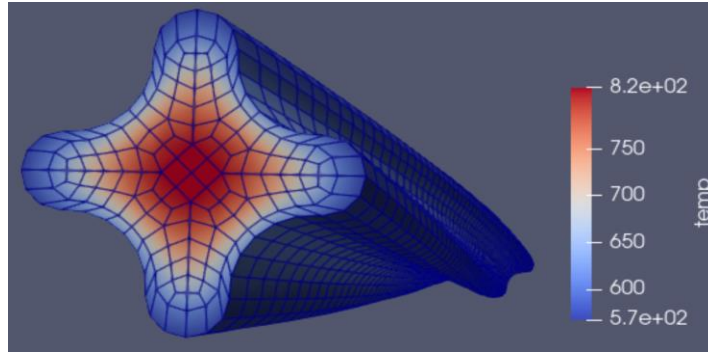


Figure 60: Temperature distribution at the time of peak fuel temperature

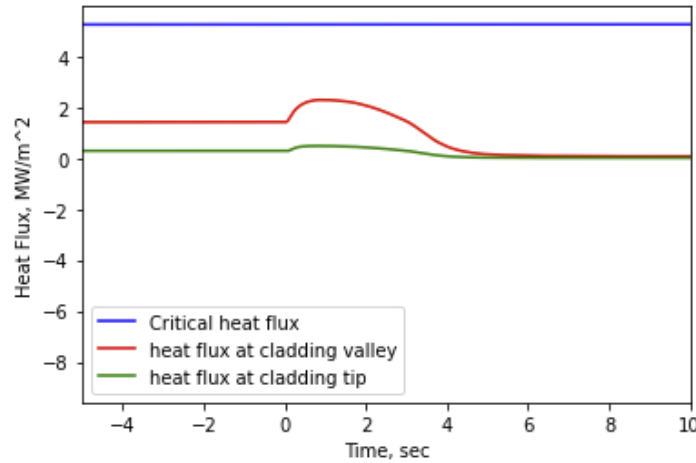


Figure 61: Cladding surface output heat flux in comparison to critical heat flux

The fuel and cladding mechanical responses are examined for two conditions: a) lateral movement is constrained by rod-to-rod contact, and b) fuel rod expansion without constraints. Figure 62 shows the von-Mises stresses at the cladding valley and cladding tip locations for the rod-to-rod contact case, and Figure 63 shows the results without rod-to-rod contact. Figure 64 shows the cladding stress contour at the peak condition.

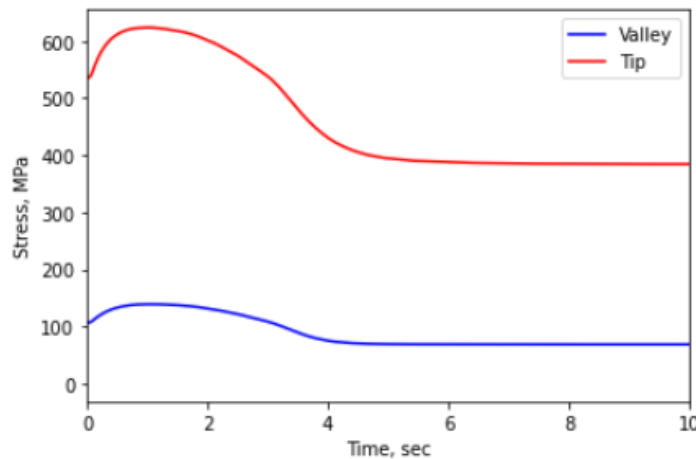


Figure 62: Cladding von-Mises stresses (rod-to-rod contact)

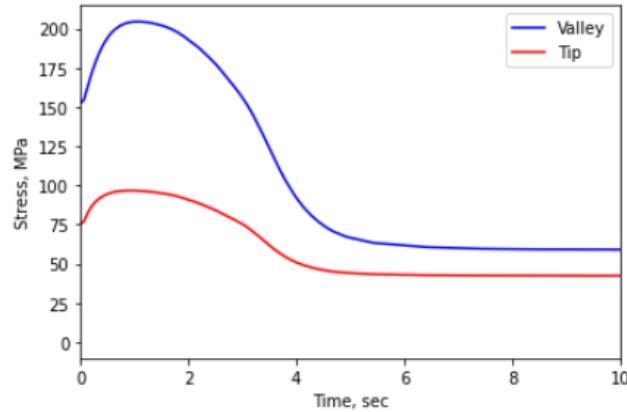


Figure 63: Cladding von-Mises stresses (no constraints)

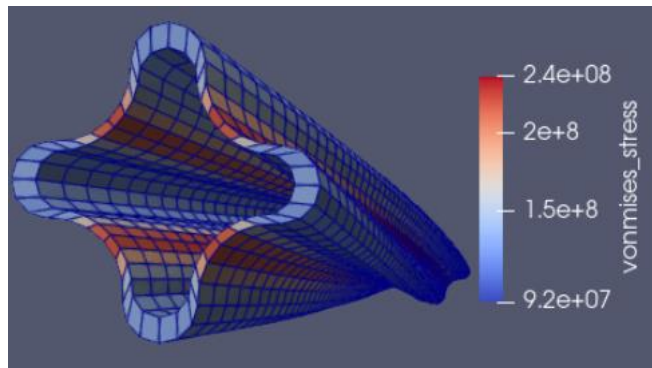


Figure 64: Cladding von-Mises stress contours at the time of peak fuel temperature

The large von-Mises stress at the cladding tip is primarily due to the constraint by rod-to-rod contact, and the stress is primarily compressive, therefore, it is not of much concern on affecting the cladding integrity. The von-Mises stress at the valley location is more significant in the case without constraint, and the three stress components are plotted in Figure 65 below. Note that all those positive values indicate the cladding under tensile state. This is presumably caused by the thermal expansion of fuel. Those stresses are still much lower than the cladding yield stress.

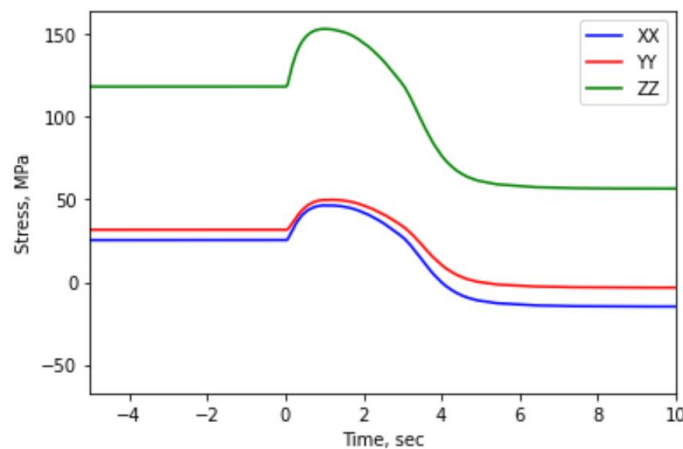


Figure 65: Cladding stresses at the valley location

Figure 66 shows the cladding hoop strain and axial strain at the valley location. The maximum hoop strain is 0.43% and difference between the peak power and full power condition is only 0.2%. The

axial strain is slightly lower than the hoop strain. Those small strains are consistent with the stresses. Overall, the fuel response in the accident does not seem to exhibit significant mechanical load. However, it should be noted, that, this result is for accident condition modeling for a fuel without prior irradiation history. Irradiated fuel rod would have additional mechanical load due to the fuel swelling.

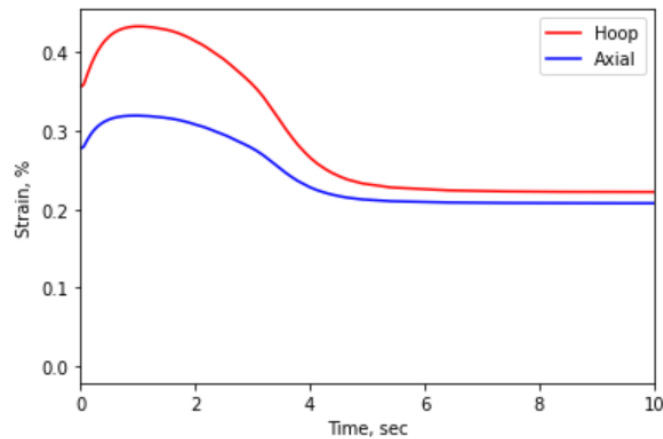


Figure 66: Cladding hoop and axial strains at the valley location

5.2.3 REA HZP Case

A control rod ejection accident at hot zero power (HZP) condition is also modeled using BISON. Figure 67 plots the rod linear in the accident condition. The input power history and axial peaking factors are based on analysis case for light water reactor UO_2 fuel and zircaloy cladding. The maximum axial peaking factor is 2.0 (at 3.14 m) during the transient. A 3-D segment is modeled at the location of axial peaking, which is close to the coolant channel outlet location. Figure 68 plots the coolant temperature calculated using BISON code from the modeling of a full-length fuel rod problem.

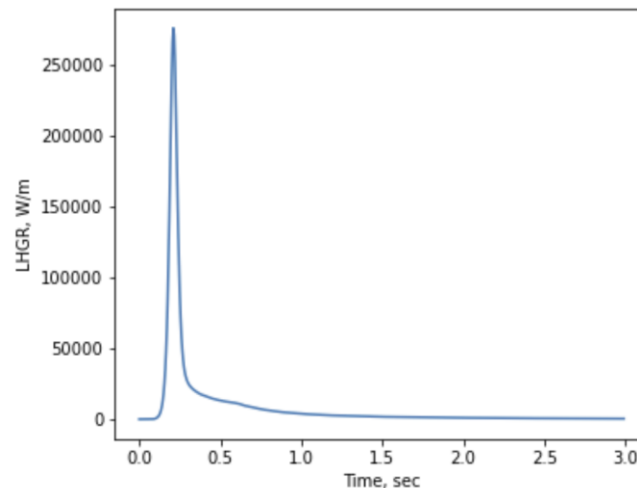


Figure 67: Rod linear power in a control rod ejection accident

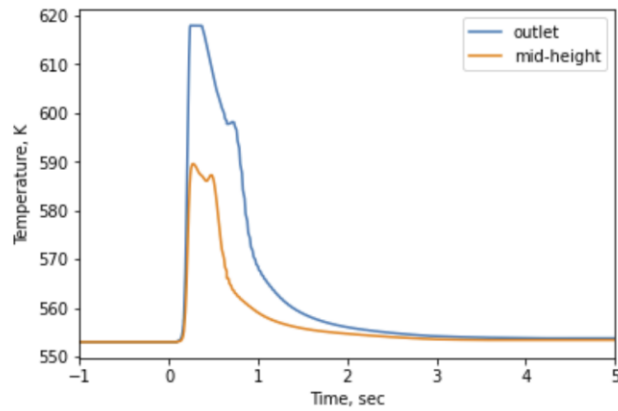


Figure 68: Coolant temperature calculated by BISON code

5.2.4 REA HZP Results

Figure 69– Figure 71 show the peak fuel temperature, cladding temperatures at the valley and tip locations and cladding heat flux in comparison to the critical heat flux.

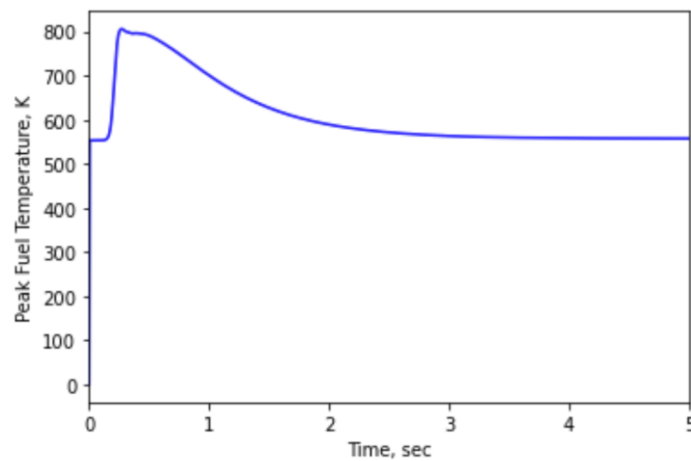


Figure 69: Peak fuel temperature during the REA at HZP

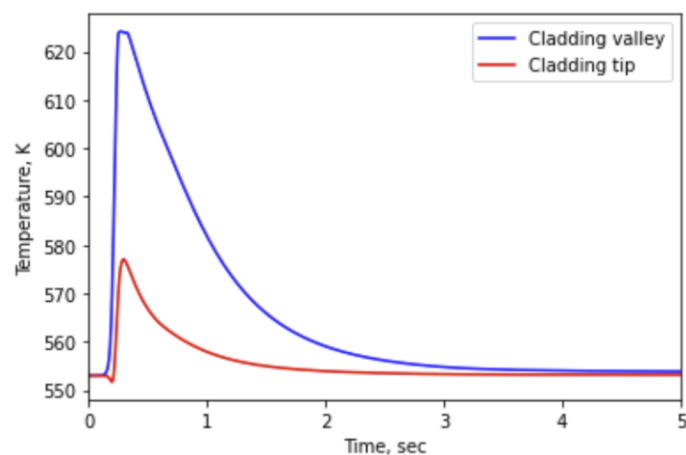


Figure 70: Cladding temperatures at the valley and tip during the REA at HZP

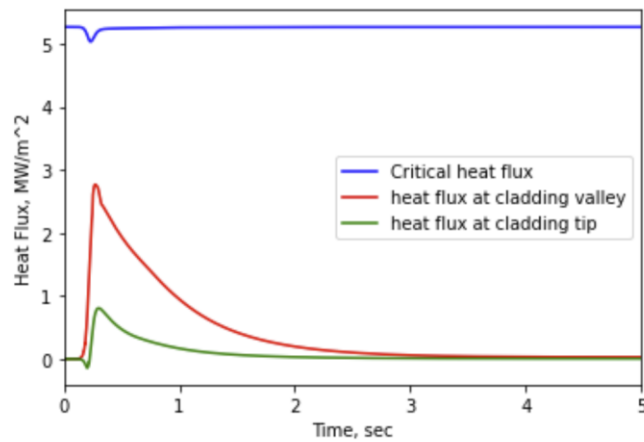


Figure 71: Heat flux at the cladding valley and tip in comparison to the critical heat flux

Figure 72 and Figure 73 show the cladding von-Mises stresses at the valley and tip locations with two different boundary conditions: a) constraint due to rod-to-rod contact and b) no constraint. Similar responses are shown as the HFP case. Again, the high stress at the cladding lobe tip in case a) is mainly due to the constraint of thermal expansion in the radial direction.

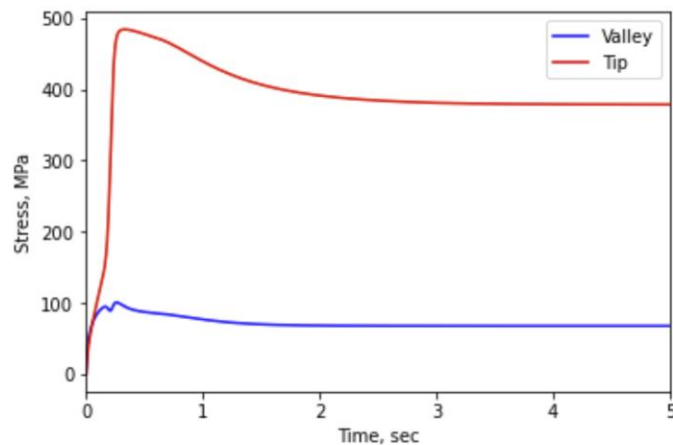


Figure 72: Cladding von-Mises stress at the valley and tip locations during the REA at HZP condition with rod-to-rod contact

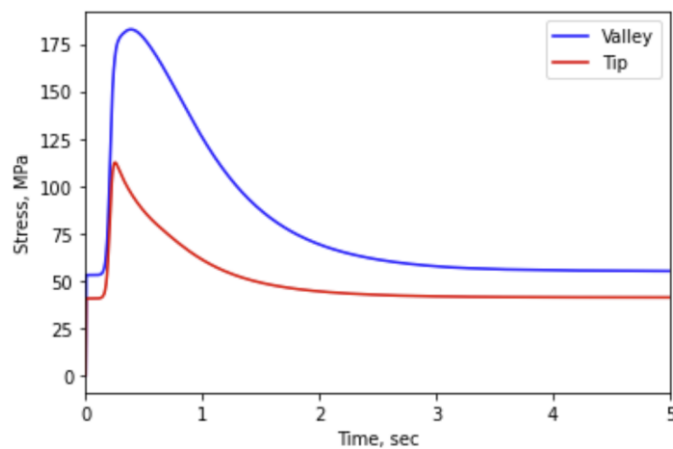


Figure 73: Cladding von-Mises stress at the valley and tip locations during the REA at HZP condition without rod-to-rod contact

Figure 74 examines the stress components in X, Y, and Z directions. The positive value indicates the tensile nature of the stresses at the valley. The cladding hoop and axial strains at the valley location are shown in Figure 75. The peak value of hoop strain is 0.42%, which is slightly larger than the axial strain.

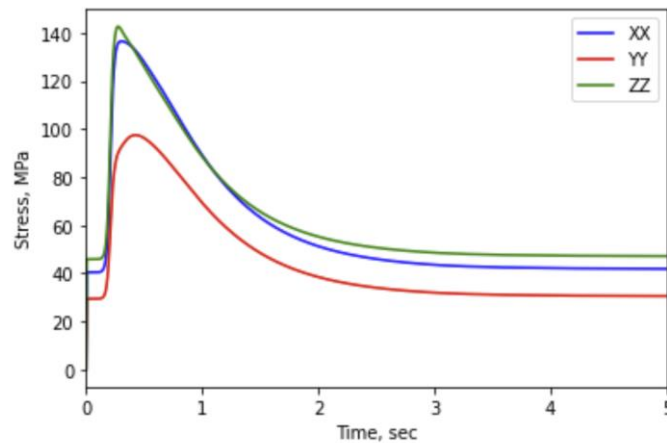


Figure 74: Cladding stress components at the valley location without rod-to-rod contact

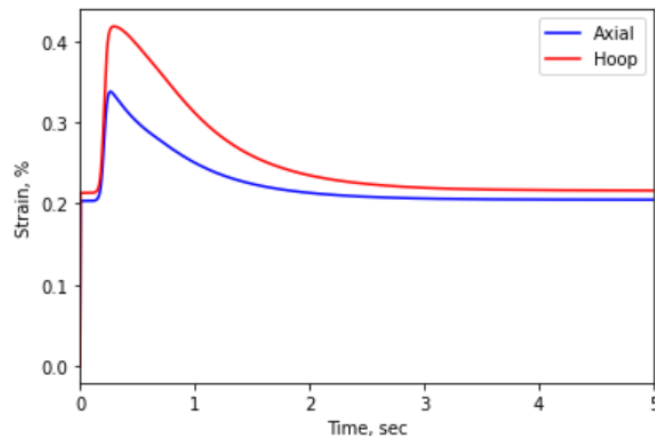


Figure 75: Cladding hoop and axial strains at the valley location

5.2.5 Fuel Failure Discussion

In those accident conditions, the main concern is the determination of the fuel failure condition based on the results of fuel performance modeling. Since there is no relevant test data available, the discussions here deal in general with the concerns for conventional UO_2 fuel and the relevance of those concerns and related failure mechanisms to the metal fuel.

In the event of large energy deposition in the fuel due to reactivity insertion, one type of fuel failure is associated with the high surface heat flux that results in the DNB at cladding surface, and this could cause sustained high temperatures and damages the cladding; conservatively, the occurrence of DNB is usually assumed to be the fuel failure limit, and this can still be used for this type of fuel. The special geometry in this metal fuel could have less margin to DNB due to its high local heat flux.

However, mechanical failure does not necessarily occur at DNB, as has been shown in many simulated RIA tests on UO_2 fuel. Since this metallic fuel design could not have rod ballooning, and the stored energy in the fuel is lower than ceramic fuel, it is still possible to have fuel rewetting to mitigate the consequence of DNB should it occur. Current modeling results did not reach the DNB limit and post-DNB behavior was not modelled.

The zirconium-alloy cladding of the metal fuel will have the same corrosion and hydrogen uptake issues in the water reactor environment as the conventional UO_2 fuel cladding. Therefore, the reduction of cladding ductility is expected to be similar to other zirconium cladding alloys operated at same conditions. Although this metal fuel does not have pellet-cladding interaction issues, in fast power transient, the mechanical failure might be assumed to occur when the cladding deformation strain exceeds a failure limit of cladding. That failure limit might be inferred from mechanical tests should they become available. The calculations indicate there is very limited deformation in the cladding driven by fuel thermal expansion in the accident condition for the fresh fuel cases modelled. For irradiated fuel, the assessment needs to account for pre-existing stresses/strains in the cladding due to fuel swelling in the assessment of fuel failures. As shown from results on the normal operation condition in Section 3, the fuel swelling could continuously push the cladding, and if the cladding stress is not adequately relieved, the margin to the yield point of the cladding might be lower, and this also indicates a lower margin to fuel cladding breach. Furthermore, the cladding ductility is expected to be lower for the high burnup fuel with long residence time in core. With all those combined, the end-of-life condition could be more limiting: the swelling could be significant, and the cladding ductility would be minimal due to corrosion and irradiation.

In comparison of the fuel responses between the HZP and HFP conditions, although the power pulse width might differ, and the narrow power pulse at a HZP condition could cause a higher heating rate of the fuel, both HZP and HFP modeling results are very similar in that the mechanical load is driven by the thermal expansion of fuel core.

The phase diagram in Section 2 has shown that the metal fuel has a relatively lower melting temperature as compared to the ceramic UO_2 fuel, the power to melting is not computed for the metal fuel as a fuel performance metric. As can be seen from current results, fuel melting cannot occur in the over-power transients without having a DNB first. In the event that the critical heat flux is reached and a temperature escalation on the cladding surface has occurred, the temperature drop across the fuel is not significant, and the failure mechanisms would still be bounded by either the softening of the fuel or the cladding damage.

6. CONCLUSIONS

Using metal fuel in LWR environment is rather revolutionary to the current nuclear commercial fleet that is dominated by the ceramic UO_2 fuel. It offers potential enhanced safety in accident conditions but needs analytical and experimental work to confirm its feasibility in commercial reactor applications.

Current work, using the modeling simulation tool BISON developed in the U.S. DOE's NEAMS program, models the metal fuel behavior in LWRs in operation and accident conditions. Particularly, a helical geometry fuel with four-lobe cross-section by Lightbridge Corp. has been used as the subject of the study.

A few new material models have been adopted/developed using open literature data and implemented in BISON code. The implementation includes all the thermal and mechanical property models of UZr_2 , an alloy that is used as the fuel material, an adoption of an oxidation model for Zr-Nb cladding alloy to provide a better estimate of the cladding corrosion and hydrogen uptake, and BISON code modifications to augment the efficiency on the fuel modeling in 2D/3D geometry.

Finite element grids for both 2-D planar geometry and 3-D segments were created. A new modeling method that uses multiple 2-D planes was developed for modeling the full-length fuel rod response.

The responses of metallic fuel under operational and accident conditions, with either a loss of coolant or a rapid power increase using a few idealized cases, were modelled using the modified BISON code with new material models.

In comparison to the ceramic UO_2 fuel, the enhanced safety of metallic fuel is clearly shown in the results of accident conditions. This metallic fuel design has no free volume; therefore, it eliminates several issues such as the cladding lift-off due to over-pressure or the cladding ballooning and burst in accident conditions. The fuel temperature in both operation and accident conditions remain much lower than UO_2 fuel, which lowers the temperature and reduces oxidation in the cladding when the surface heat transfer deteriorates due to the loss of cooling. The cladding stresses under the accident conditions with rapid power changes could increase, but not significantly, due to limited fuel thermal expansion.

The performance concern of this metal fuel design would mainly be its relatively larger dimensional changes due to swelling and the effects on cladding ductility of corrosion and irradiation. The fuel swelling would have implications: a) adding mechanical load to the cladding and reduction of its margin to cladding fracture/breach under normal operations and accident conditions, and b) the potential interference with other components in the fuel assembly.

In examining the fuel performance modeling results, a few notable features were found due to the special geometry: cladding output heat flux and oxidation peak at the valley location, and cladding stress/strains are not uniform along the circumference. The non-uniformity in heat flux or corrosion may reduce some margins as compared to a reference cylindrical geometry, but those effects should be secondary.

The metallic fuel study was focused on the special helical geometry using the UZr_2 fuel material. Alternative design could possibly be used to improve the fuel performance should a different geometry or material be used. BISON code can be used to vary the design and material parameters for optimizing the fuel design. Those could be pursued in the future.

Current modeling approach uses open literature information to develop new models that could best represent the properties of the metal fuel but, in some cases, the existing information/data could not be readily reconciled, and the measurement data could be scarce for some properties; therefore, large

uncertainties in some models should be acknowledged. In particular, the fuel swelling could have significant impact on the performance; however, little data is available about the swelling characteristics of δ -phase U-Zr alloy. Experimental work in the future can perhaps provide information that improves the material modeling and code validation.

Current modeling results presented are certainly not conclusive. All studies are performed within the domain of fuel performance modeling, and simplification and assumptions were made along the way. This does not prevent a more refined study in the future should more information becomes available on the core/fuel characteristics and coupling with thermal-hydraulics and neutronics codes.

Given the little information that is available for the performance study conducted for this particular fuel design, we hope that through this work, the evaluation of metal fuel be continued through modeling and simulation; we recommend and encourage further quantitative evaluation of the performance of a new fuel design, taking advantage of the material models employed, modeling approach adopted, and assumptions made.

We hope this report, through its contribution to filling the gap in metal fuel modeling and by providing insights on metal fuel performance issues in LWR environments, has fulfilled the mission perceived for this project.

7. ACKNOWLEDGEMENT

This work was funded by U.S. Department of Energy (DOE) under award number DE-NE0009041. The computation conducted in the work made use of Idaho National Laboratory's High Performance Computing systems located at the Collaborative Computing Center and supported by the Office of Nuclear Energy of the U.S. DOE and the Nuclear Science User Facilities under Contract No. DE-AC07-05ID14517.

8. REFERENCES

1. A. Bostrom, et. al., “Development and Properties of Uranium-Base Alloys Corrosion Resistant in High Temperature Water, Part I - Alloys without Protective Cladding,” WAPD-127, Part I, April 25, 1955
2. I. Cohen, et al., “Development and Properties of Uranium-Base Alloys Corrosion Resistant in High Temperature Water Part II – Alloys with Protective Cladding”, WAPD-127, September 1955
3. L. Bleiberg, et. al. “Development and Properties of Uranium-Base Alloys Corrosion Resistant in High Temperature Water, Part IV - Radiation Stability of Uranium-base Alloys,” WAPD-127, Part IV, May 1957
4. Willard, R.M. and Schmitt, A.R., “Irradiation Swelling, Phase Reversion, and Intergranular Cracking of U-10wt%Mo Fuel Alloy,” NAA-SR-8956, Atomics International, Canoga Park, CA, 1965
5. L.L.J. Marsh, Strength characteristics of zirconium-uranium alloys, in: F.A. Rough (Ed.) An Evaluation of Data on Zirconium-Uranium Alloys (Report BMI-1030), Battelle Memorial Institute, Columbus, OH, 1955, pp. 47-68
6. L.L.J. Marsh, Strength characteristics of uranium-zirconium alloys, in: A.A. Bauer (Ed.) An Evaluation of the Properties and Behavior of Zirconium-Uranium Alloys (Report BMI-1350), Battelle Memorial Institute, Columbus, OH, 1959, pp. 55-77
7. O. Reistad, et. al. “Russian Nuclear Power Plants for Marine Applications,” NKS-138, Apr. 2006
8. R. McDonell and E. F. Sturcken, “Development of High Performance Uranium Metal Fuels for Savannah River Reactors,” ANS Winter Meeting, San Francisco, Nov. 11-16, 1973
9. R. Montgomery, et. al., “An Innovative Accident Tolerant LWR Fuel Rod Design Based on Uranium-Molybdenum Metal Alloy,” TOPFUEL 2006
10. Standard Review Plan (NUREG-0800) Chapter 4.2
11. C. Hartmann, A. Totemeier, S. Holcomb, J. Liverad, M. Limi, J.E. Hansen and E. Navestad, *Measurement Station for Interim Inspections of Lightbridge Metallic Fuel Rods at the Halden Boiling Water Reactor*, EPJ Web of Conferences 170, 04011 (2018)
12. Transcript of the ACRS Thermal-Hydraulics Phenomena Subcommittee, August 21, 2018, NRC-3858, ADAMS ML18254A164
13. US Patent 10,991,473 B2, Bashkirtsev et al., “Method of Manufacturing a Nuclear Fuel Assembly,” April 27, 2021
14. US Patent 2011/0255651 A1, Bashkirtsev et al., “Nuclear Reactor (Alternatives), Fuel Assembly of Seed-Blanket Subassemblies for Nuclear Reactor (Alternatives), and Fuel Element for Fuel Assembly,” Oct. 20, 2011
15. US Patent 9,355,747 B2, Bashkirtsev et al., “Light Water Reactor Fuel Assembly (Alternatives), A Light Water Reactor, and a Fuel Element of Fuel Assembly,” May 31, 2016

16. *Lightbridge Fuel™ Development Program*, ADAMS ML18232A126
17. A. Totemeier, *Lightbridge Fuel™ Overview*, Spring 2021 Nuclear Waste Technical Review Board Meeting, May 12, 2021
18. Yu. V. Petrov, A. N. Erykalov, and M. S. Onegin, “The Fuel Cycle of Reactor PIK,” International Meeting on Reduced Enrichment for Research and Test Reactors, Nov. 3-8, 2002, Bariloche, Argentina
19. T. M. Conboy, T. J. McKrell & M. S. Kazimi, Experimental Investigation of Hydraulics and Lateral Mixing for Helical-Cruciform Fuel Rod Assemblies, *Nuclear Technology*, 182:3, 259-273, 2013
20. T. M. Conboy, T. J. McKrell & M. S. Kazimi, “Evaluation of Helical-Cruciform Fuel Rod Assemblies for High-Power-Density LWRs,” *Nuclear Technology*, 188:2, 139-153, 2014.
21. D. Feng., “Innovative Fuel Designs for High Power Density Pressurized Water Reactor,” Ph.D. Dissertation, 2005
22. Janney, Dawn E. *Metallic Fuels Handbook, Part 1: Alloys Based on U-Zr, Pu-Zr, U-Pu, or U-Pu-Zr, Including Those with Minor Actinides (Np, Am, Cm), Rare-earth Elements (La, Ce, Pr, Nd, Gd), and Y*, 2018-08, INL/EXT-15-36520
23. G. L. Hofman, M. C. Billone, J. F. Koenig, J. M. Kramer, J. D. B. Lambert, L. Leibowitz, Y. Orechwa, D. R. Pedersen, D. L. Porter, H. Tsai, and A. E. Wright. *Metallic fuels handbook*. Technical Report ANL-NSE-3, Argonne National Laboratory, 2019
24. Y.S. Touloukian, R.W. Powell, C.Y. Ho, P.G. Klemens, *Thermal Conductivity (Thermophysical Properties of Matter vol. 1)*, IFI/Plenum, New York, 1970
25. Y. Takahashi, M. Yamawaki, K. Yamamoto, *Thermophysical Properties of Uranium-Zirconium Alloys*, *Journal of Nuclear Materials*, 154 (1988), p. 141-144
26. S. Kaity, J. Banerjee, M.R. Nair, K. Ravi, S. Dash, T.R.G. Kutty, A. Kumar, R.P. Singh, *Microstructural and Thermophysical Properties of U-6 wt.%Zr alloy for Fast Reactor Application*, *Journal of Nuclear Materials*, 427 (2012), p. 1-11
27. Y. Takahashi, K. Yamamoto, T. Ohsato, H. Shimada, T. Terai, M. Yamawaki, *Heat Capacities of Uranium-Zirconium Alloys from 300 to 1100 K*, *Journal of Nuclear Materials*, 167 (1989), p.147-151
28. G.B. Fedorov, E.A. Smirnov, *Heat Capacity of Uranium-Zirconium Systems*, *Soviet Journal of Atomic Energy*, 25 (1968) 795-797 (translated from *Atomnaya Énergiya* vol 725 no. 791 p. 754-756, July 1968
29. Lee, et. al., “Measurement of Specific Heat of Zr-40 wt% U metallic fuel,” *Journal of Nuclear Material*, 360, (2007), p. 315-320
30. T.R.G. Kutty, C.B. Basak, A. Kumar, H.S. Kamath, *Creep behavior of delta-phase of U-Zr system by impression creep technique*, *Journal of Nuclear Materials*, 408 (2011), p. 90-95
31. Bagchi AC, Prasad GJ, Khan KB and Singh RP, “Physical Metallurgical Studies of Zr-Rich U-Zr Alloys,” *Journal of Material Sciences and Engineering*, 2013, 2:1

32. AM Yacout and MC Billone. Current status of the life fast reactors fuel performance codes. In Fast Reactors and Related Fuel Cycles: Safe Technologies and Sustainable Scenarios (FR13). COMPANION CD-ROM. Proceedings of an International Conference. 2015
33. T. Ogata and T. Yokoo, “Development and Validation of ALFUS: An Irradiation Behavior Analysis Code for Metallic Fast Reactor Fuels,” *Journal of Nuclear Technology*, 128(1), 1999, p. 113–123
34. A. Karahan and J. Buongiorno, “A New Code for Predicting the Thermo-mechanical and Irradiation Behavior of Metallic Fuels in Sodium Fast Reactors,” *Journal of Nuclear Materials*, 396, 2010, p. 283-293
35. Idaho National Laboratory, “BISON A Finite Element-Based Nuclear Fuel Performance Code,” <https://mooseframework.inl.gov/bison/index.html>
36. C. M. Allison, et. al. SCDAP/RELAP5/MOD3.1 code manual, volume IV: MATPRO—A Library of Materials Properties for Light-Water-Reactor Accident Analysis. Technical Report NUREG/CR-6150, EGG-2720, Idaho National Engineering Laboratory, 1993
37. A. Shestopalov, K. Lioutov, and L. Yegorova, “Adaptation of USNRC’s FRAPTRAN and IRSN’s SCANAIR Transient Codes and Updating of MATPRO Package for Modeling of LOCA and RIA Validation Cases with Zr-1%Nb (VVER Type) Cladding”, NUREG/IA-0209, April, 2003
38. L. Yegorova, et. al., “Data Base on the Behavior of High Burnup Fuel Rods with Zr-1%Nb Cladding and UO₂ Fuel (VVER Type) under Reactivity Accident Conditions,” NUREG/IA-0156, Vol. 2, 1999
39. K. Geelhood and C. Beyer, “Hydrogen Pickup Models for Zircaloy-2, Zircaloy-4, M5TM and ZIRLOTM,” 2011 Water Reactor Fuel Performance Meeting, Chengdu, China, September 11-14, 2011, Paper T2-011
40. L.O. Jernkvist and A.R. Massih, Models for Fuel Rod Behavior at High Burnup, SKI Report 2005:41, December 2004
41. J. Malone, A. Totemeier, N. Shapiro, S. Vaidyanathan, “Lightbridge Corporation's Advanced Metallic Fuel for Light Water Reactors,” *Nuclear Technology* 180 (2012), p. 437–442
42. D. Pizzocri, G. Pastore, T. Barani, A. Magni, L. Luzzi, P. Van Buffelen, S.A. Pitts, A. Alfonsi, and J.D. Hales, “A Model Describing Intra-granular Fission Gas Behavior in Oxide Fuel for Advanced Engineering Tools”, *Journal of Nuclear Materials*, **502** (2018), p. 323-330
43. G. Pastore, N. Militello, S. Blondel, and B.D. Wirth, “Single-size and Cluster Dynamics Modeling of Intra-granular Fission Gas Bubbles in UO₂”, *Journal of Nuclear Materials* (2022) under review.
44. K.J. Geelhood, W.G. Luscher, P.A. Raynaud and I.E. Porter, “FRAPCON-4.0: A Computer Code for the Calculation of Steady-State, Thermal-Mechanical Behavior of Oxide Fuel Rods for High Burnup,” PNNL-19418, Vol. 1 Rev. 2, September 2015, ML16118A427
45. K. Geelhood and C. Beyer, “Corrosion and Hydrogen Pickup Modeling in Zirconium Based Alloys,” 2008 Water Reactor Fuel Performance Meeting, Seoul, Korea, October 19-23, 2008, Paper 8145

46. Arthur Motta, et.al., “Hydrogen in Zirconium Alloys: A review”, *Journal of Nuclear Materials* 518 (2019) p.440-460
47. Adrien Couet, Arthur T. Motta, Robert J. Comstock, “Hydrogen Pickup Measurements in Zirconium alloys: Relation to Oxidation Kinetics”, *Journal of Nuclear Materials* 451 (2014), p. 1–13
48. A.T. Motta, M.J. Gomes Da Silva, A. Yilmazbayhan, R.J. Comstock, Z. Cai, B. Lai, “Microstructural Characterization of Oxides Formed on Model Zr Alloys Using Synchrotron Radiation”, *Zirconium in the Nuclear Industry: 15th International Symposium*, ASTM STP 1505, 2009, p. 486
49. J.G. Collier, “Convective Boiling and Condensation,” McGraw-Hill, 1981
50. F. F. Cadek, D. P. Dominicis, H. C. Yeh, and R. H. Leyse, “PWR FLECHT Final Report Supplement,” WCAP-7931, Oct. 1972
51. Y. Deng, K. Shirvan, Y. Wu, and G. Su, “Utilization of 3D Fuel Modeling Capability of BISON to Derive New Insights in Performance of Advanced PWR Fuel Concepts,” *Journal of Nuclear Materials*, vol 519, 2019, p. 271-288

APPENDIX A SCRIPT FOR COMPUTING GEOMETRY PARAMETERS OF HELICAL FOUR-LOBE FUEL

```
In [1]: import numpy as np
import matplotlib.pyplot as plt
```

```
In [2]: rf = 1.2           # inner radius of curvature at lobe
Delta = 1.53*2.0          # lobe thickness
r = 1.49                  # outer radius of curvature at lobe
r = Delta/2.0
D = 12.6                  # diameter
Rc = D / 2.0
Dv = 6.75
Rv = 3.26                 # radius of curvature at valleys
d0 = 0.4                  # thickness of cladding at valleys
dmax = 1.02               # thickness of cladding at end of lobes
a = 1.56                  # displacer width
```

In [3]:

```

# coordinates at the outer surface of cladding Lobe
x0 = Rc;      y0 = 0.0

# coordinates at the connection point between valley and lobe on outer cladding surface
y1 = Delta/2.0;      x1 = Rc - (r - np.sqrt(r**2.0 - y1**2.0))

# coordinates at the inner surface of cladding Lobe
x2 = Rc - dmax;      y2 = 0.0      #

# coordinates at the connection point between valley and lobe on inner cladding surface
y3 = Delta/2.0 - d0;  x3 = x2 - (rf - np.sqrt(rf**2.0 - y3**2.0))

d1 = (y1 - x1)/np.sqrt(2.0) # distance to the line of symmetry
d3 = (y3 - x3)/np.sqrt(2.0) # distance to the line of symmetry
L1 = np.sqrt(x1*x1 + y1*y1 - d1*d1)
L3 = np.sqrt(x3*x3 + y3*y3 - d3*d3)

L2 = Dv/2.0
L4 = L2 - d0

x4=L2/np.sqrt(2)
y4 = x4
x5 = L4/np.sqrt(2)
y5 = x5

```

```

In [4]: p0 = (x0, y0)
p1 = (x1, y1)
p2 = (x2, y2) p3
= (x3, y3)
p4 = (x4, y4)
p5 = (x5, y5)

plt.figure()
plt.xlabel('x, mm')
plt.ylabel('y, mm')
for i, p in enumerate( [p0,p1,p4,p2,p3,p5] ):
    print(f"{p[0]: .3f},{p[1]: .3f}")
    plt.scatter(p[0], p[1])
    plt.text(p[0], p[1], str(i))
    pold = p

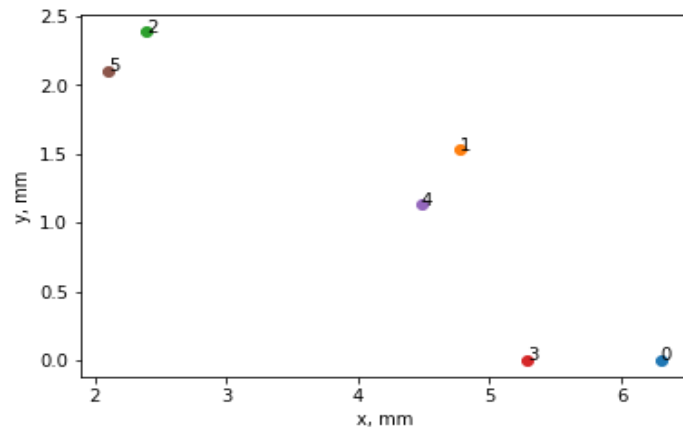
plt.show()

```

```

6.300, 0.000
4.770, 1.530
2.386, 2.386
5.280, 0.000
4.484, 1.130
2.104, 2.104

```



In [5]:

```

# compute radius of curvature
d1_square = (y1 - x1)**2.0/2.0

h1 = np.sqrt( x1**2.0 + y1**2.0 - (y1 - x1)**2.0 /2.0 ) - L2

R1 = (h1**2.0 +d1_square)/(2*h1)
R1
d2_square = (y3 - x3)**2.0/2.0
h2 = np.sqrt(x3**2.0+y3**2.0 - d2_square) - L4

R2 = (h2**2.0+d2_square)/(2*h2)
print(f"{R2:.3f}")

xc1 = Rc - r
yc1=0
print(f"{xc1:.3f}",f"{yc1:.3f}")

xc2 = (L2 +R2) /np.sqrt(2)
yc2 = xc2
print(f"{xc2:.3f}", "{yc2:.3f}")

```

3.325

4.770 0.000

4.737 4.737

```

xc1 = Rc - dmax - rf
yc1 = 0
print(f"{R1:.3f}")
print(f"{xc1:.3f}",f"{yc1:.3f}")
xc2 = (L4+R1)/np.sqrt(2)
yc2 = xc2
print(f"{xc2:.3f}", f"{yc2:.3f}")

```

In [6]:

2.970
 4.080 0.000
 4.204 4.204

In

[7]:

```
AF = 37.49 # mm^2, fuel only
AT = 63.53 # mm^2, fuel+clad
AF = 50.1 # mm^2, fuel only
AT = 71.1 # mm^2, fuel+clad
```

```
Rf = np.sqrt(AF/np.pi)
AD = a * a # mm^2, displacer
Ri = np.sqrt(AD/np.pi)
A = AF - AD
```

```
print('# Equivalent inner radius = {:.3f} mm'.format(Ri))
print('# Total Fuel Area = {A: .2f} mm^2'.format(A=AT))
print('# Fuel Area = {A: .2f} mm^2'.format(A=AF))
print('# Fuel Area (excluding displacer) = {:.2f} mm^2 '.format(A))
print('# Equivalent outer fuel radius = {Rf: .3f} mm'.format(Rf=Rf))
Rc = np.sqrt(AT/np.pi)
print('# Equivalent outer radius = {:.3f} mm'.format(Rc))
print('# Equivalent outer diameter = {:.3f} mm'.format(Rc*2.0))
print('# Clad thickness (avg) = {:.3f} mm'.format(Rc - Rf))
```

```
# Equivalent inner radius = 0.880 mm
# Total Fuel Area = 71.10 mm^2
# Fuel Area = 50.10 mm^2
# Fuel Area (excluding displacer) = 47.67 mm^2
# Equivalent outer fuel radius = 3.993 mm
# Equivalent outer radius = 4.757 mm
# Equivalent outer diameter = 9.515 mm
# Clad thickness (avg) = 0.764 mm
```

APPENDIX B MATERIALS BLOCK IN BISON INPUT

```

[Materials]
[burnup]
  type = UPuZrBurnup
  initial_X_Zr = 0.67
  initial_X_Pu = 0.0
  density = 9870
  block = '1'
  outputs = all
  output_properties = burnup
[]
[fission_rate]
  type = UZrFissionRate
  rod_linear_power = power_history
  axial_power_profile = axial_peaking_factors
  pellet_radius      = ${fuel_outer_radius}
  pellet_inner_radius = ${fuel_inner_radius}
  axial_offset = ${axial_offset}
  outputs = all
  output_properties = fission_rate
  block = '1'
[]
[thermalUZr]
  enable = true
  type = UZrThermal
  temperature = temp
  block = '1'
  porosity = porosity
  spheat_model = utk
  thcond_model = utk
[]
[fuel_density]
  type = Density
  block = '1'
  density = 9870.0
[]
[swelling]
  type = UZrVolumetricSwellingEigenstrain
  hydrostatic_stress = hydrostatic_stress
  eigenstrain_name = 'swelling'
  output_properties = 'porosity gaseous_porosity'
  gas_swelling_scale_factor = 1.0
  gas_swelling_model = utk
  block = '1'
  outputs = all
[]

```



```

[fuel_elasticity_tensor]
  type = UZrElasticityTensor
  block = '1'
  temperature = temp
[]
[fuel_stress]
  type = ComputeMultipleInelasticStress
  block = '1'
  inelastic_models = 'fuel_creep'
[]
[fuel_creep]
  type = UZrCreepUpdate
  temperature = temp
  porosity = porosity
  fission_rate = fission_rate
  max_inelastic_increment = 1e-2
  creep_model = bmi
  block = '1'
[]
[fuel_plasticity]
  enable = false
  type = UZrPlasticityUpdate
  temperature = temp
  initial_fast_fluence = 0.0
  strain_rate = 1.0e-4
  block = '1'
[]
[fuel_thermal_expansion]
  type = UZrThermalExpansionEigenstrain
  block = '1'
  temperature = temp
  stress_free_temperature = 300.0
  eigenstrain_name = 'fuel_thermal_eigenstrain'
[]
[clad_thermal]
  type = ThermalZry
  block = '2 3'
[]
[clad_elasticity_tensor]
  type = ZryElasticityTensor
  block = '2 3'
[]
[clad_creep_model]
  type = ZryCreepLimbackHoppeUpdate
  block = '2 3'
  fast_neutron_flux = fast_neutron_flux
  temperature = temp
  zircaloy_material_type = stress_relief_annealed
  model_primary_creep = true

```

```

model_irradiation_creep = true
model_thermal_creep = true
[]
[clad_stress]
  type = ComputeMultipleInelasticStress
  block = '2 3'
  tangent_operator = elastic
  inelastic_models = 'clad_creep_model'
[]
[clad_thermal_expansion]
  type = ZryThermalExpansionMATPROEigenstrain
  block = '2 3'
  temperature = temp
  stress_free_temperature = 300.0
  eigenstrain_name = 'clad_thermal_eigenstrain'
[]
[clad_oxidation]
  type = ZryOxidation
  clad_inner_radius = ${fuel_outer_radius}
  clad_outer_radius = ${clad_outer_radius}
  temperature = temp
  fast_neutron_flux = fast_neutron_flux
  use_coolant_channel = true
  normal_operating_temperature_model = pnnl_m5
  boundary = '3'
[]
[clad_density]
  type = Density
  block = '2 3'
  density = 6551.0
[]
[]

```

APPENDIX C MESH GENERATION SCRIPTS

```

#!/python
#=====
#
# 2-D planar geometry
# Fuel Design #2 (*r2)
# Control points described in list_points
#
# size_factor = 6 (reduce to refine mesh and vice versa)
#
#
# Sideset 3 for outer surface
# Sideset 1 for x-axis
# Sideset 2 for y-axis
#
# QUAD8 Element
#
# output: 2d_r2.e
#
# Rev 1. 02/08/2022
#
#=====
f1_name = "2d_r2.e"
output_path_1 = "..\\output\\"+f1_name
auto_size_factor= 6
#=====
#
# functions

def list2str(l):
    s=""
    for a in l:
        s = s+" " + str(a)

```

```

return s

def create_vertex(list_points):
    for a in list_points:
        cubit.cmd("create vertex " + str(a[0]) + ' ' + str(a[1]))

def create_curves(list_curves):
    for a in list_curves:
        cubit.cmd("create curve vertex " + str(a[0]) + ' ' + str(a[1]))

def create_arcs(list_arcs):
    for a in list_arcs:
        cubit.cmd("create curve arc vertex " + str(a[0]) + ' ' + str(a[1]) + ' radius ' + str(a[2]) + ' normal 0 0 1 ' )

def create_surfaces(list_surfaces):
    for a in list_surfaces:
        cubit.cmd("create surface curve " + list2str(a))

list_points = [ (6.3, 0.0), (4.77, 1.53), (2.386, 2.386), (5.28, 0.0), (4.48, 1.13), (2.1036, 2.1036), (0, 0), (1.1, 0), (0.55, 0.55)]
create_vertex(list_points)

list_arcs = [(1, 2, 1.53), (3, 2, 2.97), (4,5, 1.2), (6, 5, 3.32)]
create_arcs(list_arcs)

list_curves = [(1,4), (2,5), (3,6), (7,8), (7,9), (8,9), (8,4), (9,6)]
create_curves(list_curves)

list_curves_clad = [2, 4, 3, 1, 5, 7]
list_curves_fuel = [11, 4, 3, 10, 12]
list_curves_displacer = [9, 10, 8 ]

list_surfaces = [list_curves_clad, list_curves_fuel, list_curves_displacer]

create_surfaces(list_surfaces)

```

```

cubit.cmd('delete curve 6')
cubit.cmd('merge curve all')

cubit.cmd('surface 1 2 3 copy reflect -1 1 0')
cubit.cmd('surface 1 2 3 4 5 6 copy reflect -1 0 0')
cubit.cmd('surface 1 2 3 4 5 6 7 8 9 10 11 12 copy reflect 0 -1 0')
cubit.cmd('merge curve all')

cubit.cmd('delete surface 3 6 12 9 21 24 18 15 ')
cubit.cmd('create surface curve 10 22 44 33 77 88 66 55 ')
cubit.cmd('merge curve all')

cubit.cmd('surface all size auto factor '+str(auto_size_factor))
cubit.cmd('mesh surface all')

list_vol_clad = [1, 4, 7, 10, 13, 16, 19, 22]
list_vol_fuel = [2, 5, 8, 11, 14, 17, 20, 23]
list_vol_displacer = [25]

#create blocks
cubit.cmd('block 1 surface' + list2str(list_vol_fuel))
cubit.cmd('block 2 surface' + list2str(list_vol_clad))
cubit.cmd('block 3 surface' + list2str(list_vol_displacer))
cubit.cmd('volume all scale 0.001')
cubit.cmd('block all element type QUAD8')

#create sidesets

outer_surface = [ 1, 2, 17, 18, 42, 43, 28, 29, 75, 76, 83, 84, 64, 65, 50, 51]

x_axis = [5, 11, 30, 34]
y_axis = [63, 68, 23, 19]

```

```
cubit.cmd('sideset 3 add curve' + list2str(outer_surface))  
cubit.cmd('sideset 1 add curve' + list2str(x_axis))  
cubit.cmd('sideset 2 add curve' + list2str(y_axis))  
  
cubit.cmd('export genesis"' + output_path_1 + '" dimension 2 overwrite')
```

```

#!/python
#=====
#
# 2-D plannar geometry
# Fuel Design #2 (*r2)
# Control points described in list_points
#
# size_factor = 6 (reduce to refine mesh and vice versa)
#
#
# Sideset 3 for outer surface
# Sideset 1 for x-axis
# Sideset 2 for y-axis
#
# QUAD8 Element
#
# output: multi_slice_r2.e
#
# Rev 1. 02/08/2022
#
#=====

f1_name = "multi_slice_r2.e"

#output_path_1 = "C:\\Users\\wliu\\projects\\bison_metal_fuel\\mesh\\geometry_2\\output\\"+f1_name

output_path_1 = "..\\output\\"+f1_name

auto_size_factor= 6

# Length of fuel rod
L = 100

# Number of twists

```

```

N = 20
#=====
#
# functions

def list2str(l):
    s=""
    for a in l:
        s = s+ " " + str(a)
    return s

def create_vertex(list_points):
    for a in list_points:
        cubit.cmd("create vertex " + str(a[0]) + ' ' + str(a[1]))

def create_curves(list_curves):
    for a in list_curves:
        cubit.cmd("create curve vertex " + str(a[0]) + ' ' + str(a[1]))

def create_arcs(list_arcs):
    for a in list_arcs:
        cubit.cmd("create curve arc vertex " + str(a[0]) + ' ' + str(a[1]) + ' radius ' + str(a[2]) + ' normal 0 0 1 ' )

def create_surfaces(list_surfaces):
    for a in list_surfaces:
        cubit.cmd("create surface curve " + list2str(a))

def list_add(l,n):
    l1 = []
    for a in l:
        l1.append(a+n)
    return l1

list_points = [ (6.3, 0.0), (4.77, 1.53), (2.386, 2.386), (5.28, 0.0), (4.48, 1.13), (2.1036, 2.1036), (0, 0), (1.1, 0), (0.55, 0.55)]

```



```

create_vertex(list_points)

list_arcs = [(1, 2, 1.53), (3, 2, 2.97), (4,5, 1.2), (6, 5, 3.32)]
create_arcs(list_arcs)

list_curves = [(1,4), (2,5), (3,6), (7,8), (7,9), (8,9), (8,4), (9,6)]
create_curves(list_curves)

list_curves_clad = [2, 4, 3, 1, 5, 7]
list_curves_fuel = [11, 4, 3, 10, 12]
list_curves_displacer = [9, 10, 8 ]

list_surfaces = [list_curves_clad, list_curves_fuel, list_curves_displacer]

create_surfaces(list_surfaces)

cubit.cmd('delete curve 6')
cubit.cmd('merge curve all')
cubit.cmd('surface 1 2 3 copy reflect -1 1 0')
cubit.cmd('surface 1 2 3 4 5 6 copy reflect -1 0 0')
cubit.cmd('surface 1 2 3 4 5 6 7 8 9 10 11 12 copy reflect 0 -1 0')
cubit.cmd('merge curve all')

cubit.cmd('delete surface 3 6 12 9 21 24 18 15 ')
cubit.cmd('create surface curve 10 22 44 33 77 88 66 55 ')
cubit.cmd('merge curve all')
cubit.cmd('surface all size auto factor '+str(auto_size_factor))
cubit.cmd('mesh surface all')
list_vol_clad = [1, 4, 7, 10, 13, 16, 19, 22]
list_vol_fuel = [2, 5, 8, 11, 14, 17, 20, 23]
list_vol_displacer = [25]

l0 = list_vol_clad + list_vol_fuel + list_vol_displacer
S1 = list2str(l0)

```

```

#create blocks
cubit.cmd('block 1 surface' + list2str(list_vol_fuel))
cubit.cmd('block 2 surface' + list2str(list_vol_clad))
cubit.cmd('block 3 surface' + list2str(list_vol_displacer))

for i in range(1,N+1):
    cubit.cmd('surface ' + S1 + ' copy reflect 0 0 1.0')
    N1 = list_vol_displacer[0] + (i-1)*len(l0)+1
    S2 = list2str( list(range(N1, N1+len(l0))))
    l4 = list(range(N1, N1+8))
    l5 = list(range(N1+8, N1+16))
    l6 = [N1 + 16]
    print(i)
    print(S2)
    A2 = str(45 * i)
    Z2 = str(L * i)
    print(A2)
    print(Z2)
    cubit.cmd('rotate surface ' + S2 + ' angle ' + A2 + ' about Z include_merged')
    cubit.cmd('move surface ' + S2 + ' x 0 y 0 z ' + Z2 + ' include_merged ')

    cubit.cmd("block 1 add surface " + list2str(l5) )
    cubit.cmd("block 2 add surface " + list2str(l4) )
    cubit.cmd("block 3 add surface " + list2str(l6) )

cubit.cmd('volume all scale 0.001')
cubit.cmd('block all element type QUAD8')
cubit.cmd('export genesis"' + output_path_1 + '" dimension 3 overwrite')

```

```

#!/python

f2_name = "3d_cm_n1_s4.e"
output_path_2 = "..\\output\\"+f2_name

scale = 4.0
length = 200

# functions
def list2str(l):
    s=""
    for a in l:
        s = s+" " + str(a)
    return s

def create_vertex(list_points):
    for a in list_points:
        cubit.cmd("create vertex " + str(a[0]) + ' ' + str(a[1]))

def create_curves(list_curves):
    for a in list_curves:
        cubit.cmd("create curve vertex " + str(a[0]) + ' ' + str(a[1]))

def create_arcs(list_arcs):
    for a in list_arcs:
        cubit.cmd("create curve arc vertex " + str(a[0]) + ' ' + str(a[1]) + ' radius ' + str(a[2]) + ' normal 0 0 1 ' )

def create_surfaces(list_surfaces):
    for a in list_surfaces:
        cubit.cmd("create surface curve " + list2str(a))

list_points = [ (6.3, 0.0), (4.77, 1.53), (2.386, 2.386), (5.28, 0.0), (4.48, 1.13), (2.1036, 2.1036), (0, 0), (1.1, 0), (0.55, 0.55)]
create_vertex(list_points)

```

```
list_arcs = [(1, 2, 1.53), (3, 2, 2.97), (4,5, 1.2), (6, 5, 3.32)]
create_arcs(list_arcs)
```

```
list_curves = [(1,4), (2,5), (3,6), (7,8), (7,9), (8,9), (8,4), (9,6)]
create_curves(list_curves)
```

```
list_curves_clad = [2, 4, 3, 1, 5, 7]
list_curves_fuel = [11, 4, 3, 10, 12]
list_curves_displacer = [9, 10, 8 ]
```

```
list_surfaces = [list_curves_clad, list_curves_fuel, list_curves_displacer]
```

```
create_surfaces(list_surfaces)
```

```
cubit.cmd('delete curve 6')
cubit.cmd('merge curve all')
```

```
cubit.cmd('surface 1 2 3 copy reflect -1 1 0')
cubit.cmd('surface 1 2 3 4 5 6 copy reflect -1 0 0')
cubit.cmd('surface 1 2 3 4 5 6 7 8 9 10 11 12 copy reflect 0 -1 0')
```

```
cubit.cmd('merge curve all')
cubit.cmd('delete surface 3 6 12 9 21 24 18 15 ')
cubit.cmd('create surface curve 10 22 44 33 77 88 66 55 ')
```

```
cubit.cmd('create surface curve 93 29 28 43 42 18 17 2 1 51 50 65 64 84 83 76 75')
```

```
cubit.cmd('surface all size auto factor 8')
cubit.cmd('mesh surface all')
```

```
list_vol_clad = range(26, 41, 2)
list_vol_fuel = range(27, 42, 2)
list_vol_displacer = [42]
```

```
cubit.cmd('sweep surface all helix zaxis thread_distance ' + str(length) + ' angle 90 right_handed include_mesh keep ')
```

```

cubit.cmd("volume all scale X 1 Y 1 Z " + str(scale) )

cubit.cmd('merge surface all')
cubit.cmd('merge curve all')

#create blocks
cubit.cmd('block 1 volume ' + list2str(list_vol_fuel))
cubit.cmd('block 2 volume ' + list2str(list_vol_clad))
cubit.cmd('block 3 volume ' + list2str(list_vol_displacer))
cubit.cmd('delete mesh volume 42 propagate')
cubit.cmd('merge surface all')
cubit.cmd('mesh volume 42')
cubit.cmd('volume all scale 0.001')
cubit.cmd('block all element type HEX8')

#create sidesets
list_outer_surface = [26,27,44,45,59,60,71,72,89,90,101,102,116,117, 134,135]
cubit.cmd('sideset 3 add surface' + list2str(list_outer_surface))
cubit.cmd('export genesis"' + output_path_2 + '" dimension 3 overwrite')

```